# Laser-Diode Pumped Self-Q-Switched Microchip Lasers

Jun Dong*, Ken-ichi Ueda, Hideki Yagi[1], and Alexander A. Kaminskii[2]

*Institute for Laser Science, University of Electro-Communications, 1-5-1 Chofugaoka, Chofu, Tokyo 182-8585, Japan*
[1]*Konoshima Chemical Co., Ltd., 80 Kouda, Takuma, Mitoyo-gun, Kagawa 769-1103, Japan*
[2]*Institute of Crystallography, Russian Academy of Sciences, Leninsky Prospekt 59, Moscow 119333, Russia*

Optical properties of Cr,Yb:YAG, Cr,Nd:YAG crystals, and composite Yb:YAG/Cr:YAG ceramics self-Q-switched solid-state laser materials are presented. The merits of these self-Q-switched laser materials are given and the potentials of such lasers can be chosen by the applications. Cr,Yb:YAG and composite Yb:YAG/Cr:YAG ceramics self-Q-switched laser are conducted. Although several tens of kW peak power can be obtained with a monolithic microchip Cr,Yb:YAG laser, the experimental results show that the performance of this laser is limited by the absorption of $Cr^{4+}$ ions at a pump wavelength of 940 nm and strong fluorescence quenching at high Cr concentration. Composite Yb:YAG/Cr:YAG ceramics are more suitable to realize high pulse energy and peak power (up to MW level) with optimized lasing and Q-switching parts. In addition, the instabilities induced by the multi-longitudinal mode competition in Cr,Nd:YAG and Cr,Yb:YAG microchip lasers are addressed. The different gain bandwidths of Yb:YAG and Nd:YAG play an important role in the instability of the output laser pulse trains. Stable laser pulses from the Cr,Yb:YAG microchip laser were obtained due to the antiphase dynamics. For the Cr,Nd:YAG microchip laser, the instability caused by the multi-longitudinal mode competition is an intrinsic property. Different transverse patterns were observed in Cr,Nd:YAG microchip lasers when a pump beam with larger diameter was used. Saturated inversion population distribution inside the gain medium plays an important role in the transverse pattern formation. Different transverse patterns were reconstructed by combining different sets of the Hermite–Gaussian modes. © 2008 The Optical Society of Japan

**Key words:** microchip lasers, self-Q-switched laser materials, single crystal, composite ceramics, Cr,Yb:YAG, Cr,Nd:YAG, instability of pulse oscillation

## 1. Introduction

Passively Q-switched solid-state lasers with high peak power are widely used in optical communications, pollution monitoring, nonlinear optics, material processing, medical surgery, nonlinear frequency conversion, and so on. The passively Q-switched microchip lasers are usually operated by using a thin gain medium (Nd or Yb doped material such as YAG,[1–3] $YVO_4$,[4] $KGd(WO_4)_2$,[5] or $Nd:LaSc_3(BO_3)_4$[6]) bonded with saturable absorber like a semiconductor saturable-absorber mirror (SESAM),[2,4,6] bulk $Cr^{4+}$ doped crystals,[1,3,5,7] or $Cr^{4+}$ films deposited on the gain medium by molecular beam epitaxy (MBE).[8] Compared with SESAM or the saturable absorber film deposited on the surface of the gain medium, $Cr^{4+}$ doped bulk crystals as saturable absorber have several advantages, for example, high damage threshold, low cost, and simplicity. $Cr^{4+}$:YAG crystal is widely used as Q-switch owing to its broad absorption bandwidth from 850 to 1200 nm.[9,10] For microchip passively Q-switched laser operation, optically bonding saturable absorber and gain medium is difficult to fabricate and is costly, although the laser performance of optical bonding Nd:YAG/Cr:YAG is better than those of mechanically attached Nd:YAG and Cr:YAG crystals and self-Q-switched Cr,Nd:YAG crystal.[11] The easiest way to realize such a goal is to co-dope saturable absorber and active ions into a host

material to form a self-Q-switched laser material or to use ceramic technology to form a composite structure. The Cr,Nd:YAG crystal is one of the promising self-Q-switched laser materials and microchip laser operation was demonstrated.[12–16] The advantages of Cr,Nd:YAG co-doped self-Q-switched laser crystal is that the absorption of $Cr^{4+}$ ions at the pump wavelength of a laser-diode (808 nm) is only several percent of that at 1064 nm; therefore, the absorption loss of pump power does not have great effect on the laser performance. Another advantage of Cr,Nd:YAG is that self-Q-switched laser operation can be realized at 946 nm, and a frequency-doubling laser at 473 nm can be easily generated by using an intracavity or extracavity scheme. Intracavity frequency doubling is a well-developed way to convert fundamental wavelength to green or blue in the continuous-wave operation or Q-switched laser operation with different active media, various saturable absorbers, as well as different frequency doubling nonlinear crystals.[17–20] Efficient extracavity frequency doubling generation from ultraviolet to visible range has been reported by using passively Q-switched Nd:YAG microchip lasers.[1,21–23]

Crystal growth, optical properties and a Ti:sapphire pumped self-Q-switched laser of Cr,Yb;YAG crystal have been reported.[24–27] Compared with Nd:YAG laser material, Yb:YAG crystal has several advantages such as a long storage lifetime (951 µs);[28] a very low quantum defect resulting in three times less heat generation during lasing than comparable Nd-based laser systems;[29] broad absorption bandwidth and less sensitivity to diode wavelength specifications;[30] a smaller emission cross section of

Yb:YAG suitable for obtaining high pulse energy output for Q-switching operation;[31] and easy growth of high quality and moderate concentration crystal without concentration quenching in principle.[32] Recently, highly efficient high power laser-diode pumped Yb:YAG lasers have been demonstrated.[33] Another interest in Yb:YAG lasers is that the frequency doubled wavelength of 515 nm matches the highest power line of Ar-ion lasers, thereby leading to the possibility of an all solid-state replacement.[34] Passively Q-switched Yb:YAG laser with $Cr^{4+}$:YAG as saturable absorber was first demonstrated by using a Ti:sapphire laser as pump source.[3] A passively Q-switched Yb:YAG microchip laser with 530 ps pulse width has been obtained by using SESAM.[2] A laser-diode pumped Cr,Yb:YAG microchip laser was reported,[35] however, a coating damage occurred, and no detailed information about the laser performance was given. A laser-diode pumped Cr,Yb:YAG microchip laser with pulse width of 440 ps and peak power over 53 kW has been improved by adjusting the doping concentration ratio of Yb and Cr in Cr,Yb:YAG crystal.[36] However, owing to co-doping of chromium ions with Yb into the YAG host, the fluorescence lifetime is decreased[26] with Cr concentration and there is strong absorption (about 60% of that around 1 μm) of pump power by $Cr^{4+}$ at a pump wavelength of around 940 nm; the absorbed pump power threshold is also high for compact Cr,Yb:YAG microchip laser and there is no lasing with further increase of the Cr concentration in this crystal. The passively Q-switched microchip laser configuration of a saturable absorber sandwiched between gain medium and output coupler proposed by Zayhowski *et al.* about two decades ago[1] would be an alternative way to overcome pump power absorption loss of $Cr^{4+}$ and to achieve highly efficient laser operation with short pulse width in passively Q-switched Yb:YAG/$Cr^{4+}$:YAG microchip lasers. Separation of gain medium and saturable absorber will eliminate the defects introduced in Cr,Yb:YAG crystal; $Cr^{4+}$:YAG crystal only acts as a saturable absorber, is not an additional loss to pump power which occurs in Cr,Yb:YAG crystals. Passively Q-switched Yb:YAG/Cr:YAG crystal microchip lasers with subnanosecond pulse width have been reported,[37] however, there is loss and an air gap between the interface of Cr:YAG and Yb:YAG, making the laser operation less efficient; potential energy storage of Yb:YAG cannot be fully utilized and the air gap also significantly affects the Q-switched laser performance by an etalon effect in the resonator.[38] Transparent ceramic laser materials fabricated by the vacuum sintering technique and nanocrystalline technology[39] have gained more attention as potential solid-state laser materials in recent years because they have several remarkable advantages compared with similar laser single crystals: high concentration doping, easy fabrication of large-size ceramic samples, low cost, mass production, and multilayer and multifunctional ceramic lasing components.[40,41] A highly efficient flashlamp-pumped $Cr^{3+}$ and $Nd^{3+}$ co-doped YAG ceramic laser has been demonstrated recently;[40] there has been very important research based on the sintering ceramic technology: the formation of composite materials to reduce

the thermal effect and to suppress parasitic oscillation;[42] and efficient performance of a composite Nd:YAG laser with undoped YAG as cap or clad has also been demonstrated recently.[41,43] A passively Q-switched Yb:YAG ceramic microchip laser with Cr:YAG ceramic as saturable absorber has been demonstrated,[44] output pulses with pulse energy of 30 μJ, pulse width of 380 ps and peak power of 82 kW have been obtained. Further improvement was made by increasing the transmission of output coupler and over 150 kW peak power was obtained.[45] Optical properties and laser performance of an all-ceramic composite Yb:YAG/$Cr^{4+}$:YAG self-Q-switched laser using plane-concave cavity has been reported and nanosecond pulses with pulse energy of 125 μJ and peak power of over 105 kW were measured.[46] Composite Yb:YAG/Cr:YAG ceramics not only decrease the intracavity loss between the interface of Yb:YAG and Cr:YAG, but also eliminate the air gap between these two parts, therefore, laser performance can be further improved by controlling the $Cr^{4+}$ concentration in the Cr:YAG part to realize high pulse energy output.

In this paper, we present the crystal growth of Cr,Yb:YAG and Cr,Nd:YAG co-doped self-Q-switched laser crystals; the optical properties of these crystals are measured and the effect of Cr ion introduction into Nd:YAG and Yb:YAG crystals on the optical properties and laser performance are addressed. The optical properties of composite Yb:YAG/Cr:YAG ceramics were also measured. Laser-diode pumped Cr,Yb:YAG and composite Yb:YAG/Cr:YAG ceramic microchip self-Q-switched lasers are described. The longitudinal mode competition induced instabilities in Cr,Nd:YAG self-Q-switched microchip lasers were investigated experimentally and theoretically. Pump beam diameter of laser-diode on the Cr,Nd:YAG self-Q-switched laser was investigated, and complex, high peak power transverse patterns in such lasers were observed; the effect of saturated inversion population distribution inside Cr,Nd:YAG crystal on transverse pattern formation are addressed experimentally and theoretically.

## 2. Optical Properties of Self-Q-Switched Laser Materials

### 2.1 Growth of Cr,Yb:YAG crystal

The crystal structure of YAG is cubic, the space group of YAG is $O_h^{10} - Ia3d$. The difference of lattice constant between Yb and Y is 1.5%,[47] thus, most of the Yb is substituted for the Y site in the dodecahedron coordinates in YAG crystal. Chromium ions in YAG have different valent states: divalent $Cr^{2+}$, trivalent $Cr^{3+}$, and tetravalent $Cr^{4+}$; and among them, $Cr^{3+}$ is the most stable. When Cr and Ca are introduced into the YAG crystal, there are several valent states. $Cr^{3+}$ is the dominant species and is substituted at the octahedral Al site, and $Cr^{3+}$ is the most stable valent state among Cr ions and its crystal field stabilization energy is the largest when substituted at an octahedral site. However, $Cr^{4+}$ is a saturable absorber in Cr,Yb:YAG crystal. So, controlling Cr ion valent states is the key step to obtain high $Cr^{4+}$ concentration in Cr-,Yb-codoped YAG crystal. $Cr^{4+}$ is believed to be substituted into the tetrahedral Al site,
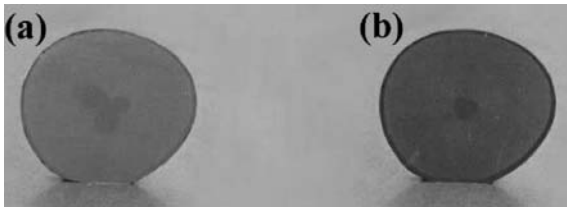
Fig. 1. Photograph of Cr,Yb:YAG crystal, (a) as-grown, (b) after annealing.

therefore a charge compensation is required which is accomplished by the substitution of $Ca^{2+}$ into the dodeca-hedral Y site. Thus, during the growth of Cr,Yb:YAG crystal, $CaCO_3$ was added as a charge compensator. Cr,Yb:YAG crystals doped with 10 at. % Yb and different Cr concentrations were grown using the Czochralski (CZ) method; the detailed growth process and annealing parameters can be found in ref. 24. Figure 1 shows a photograph of as as-grown and after annealing Cr,Yb:YAG crystals. Color of the crystal is dark after the annealing compared to that of as-grown, showing that the proper annealing condition can not only increase $Cr^{4+}$ concentration but also decrease the core area in these crystals. The growth of Cr,Nd:YAG crystals is similar to that of Cr,Yb:YAG crystal. Owing to the small segregation coefficient of Nd in YAG, only up to 1 at. % Nd can be doped into YAG crystal.

### 2.2 Optical properties of Cr,Yb:YAG and Cr,Nd:YAG crystals

The absorption and emission spectra of Cr,Yb:YAG crystal doped with 10 at. % Yb and 0.025 at. % Cr at room temperature are shown in Fig. 2, together with the absorption spectra of Yb:YAG crystal doped with 10 at. % Yb and $Cr^{4+}$:YAG crystal. There are several valent states of Cr ions in Cr:YAG crystal, $Cr^{3+}$ is the dominant state, $Cr^{4+}$ can be formed in Cr:YAG crystal by adding a $Ca^{2+}$ compensation charge, and annealing in an oxygen atmosphere. But $Cr^{4+}$ is only a small fraction (about 4%[48]) of the total Cr ions added to YAG crystals. The absorption coefficient is 12.8 cm$^{-1}$ at the peak wavelength of 941 nm for Cr,Yb:YAG crystal, higher than that for 10 at. % Yb:YAG owing to the additional absorption of $Cr^{4+}$ ions. The absorption coefficient at 1.03 μm of $Cr^{4+}$ is 1.21 cm$^{-1}$. The self-absorption of $Yb^{3+}$ at 1.03 μm was subtracted by comparing the absorption spectrum of Cr,Yb:YAG doped with 10 at. % $Yb^{3+}$ and Yb:YAG doped with 10 at. % $Yb^{3+}$. The emission spectrum of Cr,Yb:YAG crystal is identical to that of Yb:YAG crystal. The emission cross section of Cr,Yb:YAG is about $2.5 \times 10^{-20}$ cm$^2$, the fluorescence lifetime is about 584 μs,[26] which is shorter than that of Yb:YAG crystal (951 μs) due to the fluorescence quenching by the introduction of Cr ions in Cr,Yb:YAG crystal. The effect of Cr concentration on the fluorescence lifetime of Cr,Yb:YAG is shown in Fig. 3. The lifetime decreases dramatically with introduction of Cr ions into Yb:YAG crystals, then tends to decrease slowly with further increase of Cr concentration when the concentration is higher than 0.05 at. %. The cause of shortening of the
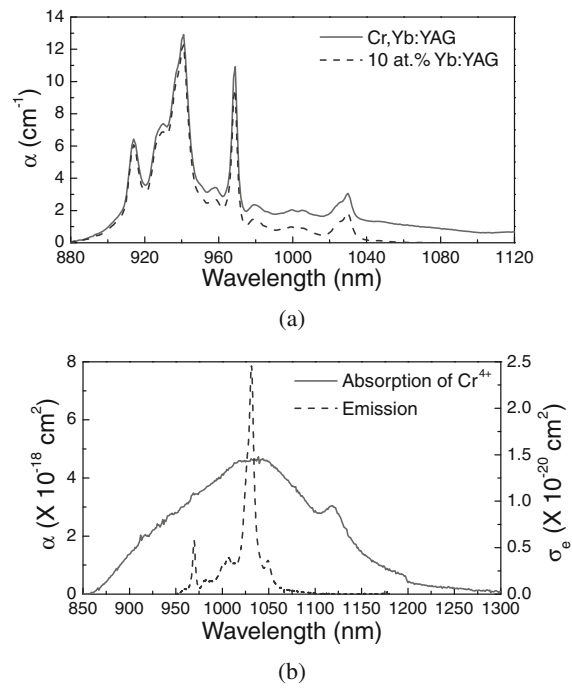


(a)



(b)

Fig. 2. (a) Absorption spectrum of Cr,Yb:YAG crystal co-doped with 10 at. % Yb and 0.025 at. % Cr, together with absorption spectrum of 10 at. % Yb:YAG crystal for comparison; (b) emission spectrum of Cr,Yb:YAG crystal and absorption spectrum of $Cr^{4+}$:YAG at room temperature.
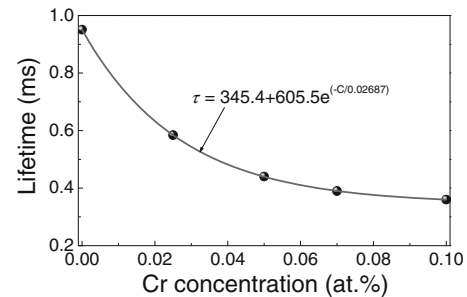


Fig. 3. Fluorescence lifetime of Cr,Yb:YAG crystals as a function of Cr concentration, the Yb doping concentration is 10 at. % for all the samples.

fluorescence lifetime of Cr,Yb:YAG is attributed to forma-tion of $Cr^{4+}$ ions and energy transfer from $Yb^{3+}$ ions to other impurities such as $Cr^{3+}$ ions. Absorption and emission spectra of Cr,Nd:YAG crystal doped with 1 at. % Nd and 0.01 at. % Cr are shown in Fig. 4. The absorption spectrum of Cr,Nd:YAG is similar to that of Nd:YAG crystal. There is a broad absorption spectrum of $Cr^{4+}$ centered at 1.06 μm. The absorption coefficient is 7.3 cm$^{-1}$ at the pumping wavelength of 808 nm for $Nd^{3+}$ ion and is 0.2 cm$^{-1}$ at 1064 nm for $Cr^{4+}$ ion. The emission spectrum of Cr,Nd:YAG is similar to that of Nd:YAG crystal, two wavelengths (946 and 1064 nm) can be emitted from Cr,Nd:YAG self-Q-switched lasers, and 946 nm microchip lasers based on Cr,Nd:YAG and second harmonic generation have been reported.[49,50] The emission cross section is
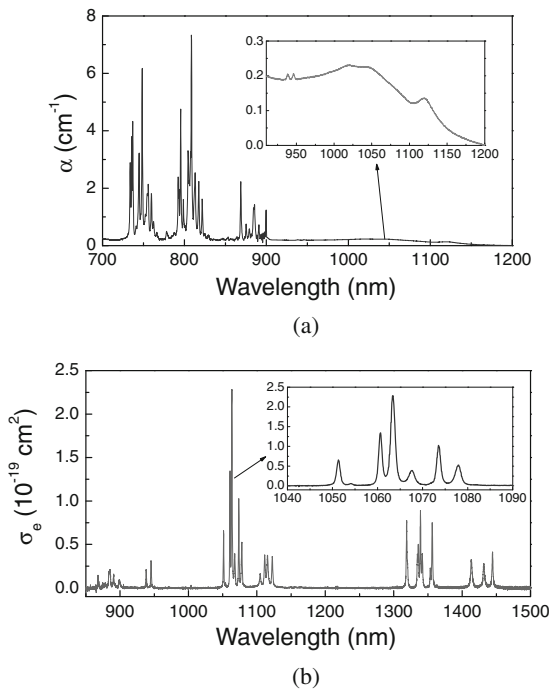
Fig. 4. Absorption and emission spectra of Cr,Nd:YAG crystal doped with 1 at. % Nd and 0.01 at. % Cr at room temperature.



Fig. 6. (a) Absorption spectra of Yb:YAG, Cr:YAG ceramics and emission spectra Yb:YAG ceramic at room temperature. (b) Measured and calculated absorptance spectra of composite Yb:YAG/Cr:YAG ceramics shown in Fig. 5.

$2.35 \times 10^{-19}$ cm$^2$ at 1064 nm, the lifetime is about 210 µs,[51] a little shorter than that of Nd:YAG (230 µs). There is almost no absorption from Cr$^{4+}$ ions at 808 nm pump wavelength for Nd:YAG, therefore, Cr$^{4+}$ ions in Cr,Nd:YAG only act as a Q-switch, and do not cuase additional loss for absorption of pump power. The laser performance of Cr,Nd:YAG self-Q-switched laser crystal is not affected by the Cr concentration, therefore, high energy can be obtained by increasing Cr concentration, as has been demonstrated by using high Cr concentration in Cr,Nd:YAG crystal in ref. 14.

### 2.3 Optical properties of composite Yb:YAG/Cr:YAG ceramics

Figure 5 shows a photograph of composite Yb:YAG/Cr:YAG ceramics fabricated by vacuum sintering technique and nanocrystalline technology.[39] The doping concentration
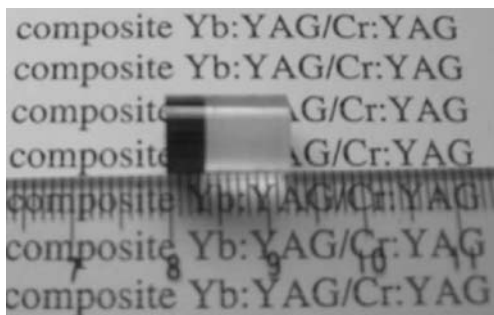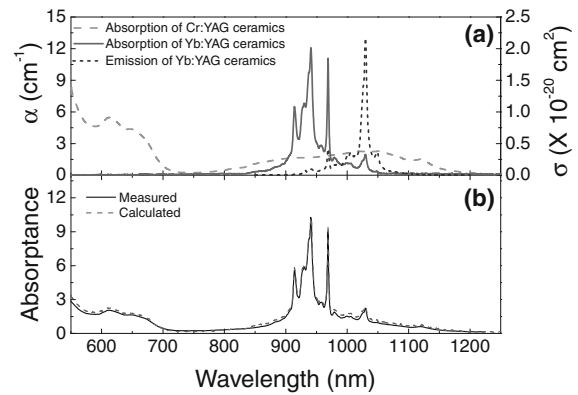


Fig. 5. Photograph of composite Yb:YAG/Cr:YAG ceramics ($\phi 8 \times 12$ mm), the thicknesses of Yb:YAG and Cr:YAG are 8 mm and 4 mm, respectively.

of Yb and Cr in composite YAG ceramics is 9.8 and 0.1 at. %, respectively. The diameter of the composite Yb:YAG/Cr:YAG ceramics is 8 mm, and thicknesses of Yb:YAG and Cr:YAG parts are 8 and 4 mm, respectively. The absorption and emission spectra of Yb:YAG/Cr:YAG composite ceramics were measured by using Yb:YAG and Cr:YAG ceramics cut from Yb:YAG/Cr:YAG composite ceramic [as shown in Fig. 6(a)]. The absorption and emission spectra of Yb:YAG ceramics are identical to those of Yb:YAG single crystals.[31] The absorption spectrum of Cr$^{4+}$:YAG ceramic is identical to that from Cr$^{4+}$:YAG single crystal previously reported.[9] There is a strong absorption at 940 nm for Cr$^{4+}$:YAG, about 70% of that at 1030 nm. The absorptance spectrum of composite Yb:YAG/Cr:YAG ceramic calculated by using the absorption spectra of Yb:YAG and Cr:YAG ceramics is in good agreement with measured absorptance spectrum of 12-mm-thick Yb:YAG/Cr:YAG composite ceramic [as shown in Fig. 6(b)].

## 3. Cr,Yb:YAG and Composite Yb:YAG/Cr:YAG Ceramics Self-Q-switched Lasers

### 3.1 Self-Q-switched Cr,Yb:YAG microchip lasers

Schematic diagrams of laser diode end-pumped Cr,Yb:YAG self-Q-switched lasers are shown in Fig. 7. Firstly, laser-diode pumped Cr,Yb:YAG microchip lasers were conducted by using a plane-concave cavity config-
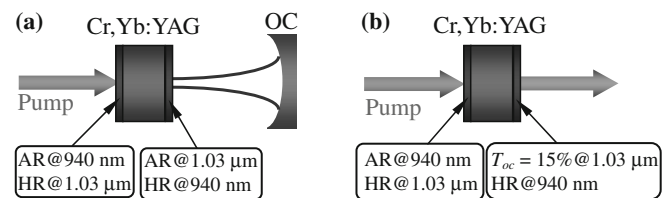


Fig. 7. Schematic diagram of laser-diode end-pumped Cr,Yb:YAG self-Q-switched lasers with (a) plane-concave cavity, and (b) monolithic microchip cavity. OC, output coupler.

uration [as shown in Fig. 7(a)]. Four Cr,Yb:YAG crystals were used in the experiments, the concentration of Yb was 10 at. %, and Cr concentration was 0.025, 0.05, 0.07, and 0.1 at. %, respectively; Crystal thickness was 1 mm. Cr,Yb: YAG samples were plane-parallel polished, one surface of the crystal was coated for anti-reflection at 940 nm and total reflection at 1030 nm to act as a cavity mirror of the laser; the other surface was coated for anti-reflection at 1030 nm to reduce the cavity loss and total reflection at 940 nm to increase the absorbed pump power. The output coupler was a concave mirror with 70 mm curvature and reflectivity was 98% and 95% at 1.03 μm; overall cavity length was ~35 mm. For monolithic microchip laser operation, coating with 15% transmission at 1030 nm was applied directly on the front surface of the Cr,Yb:YAG crystals [shown in Fig. 7(b)]. A fiber-coupled 940 nm multi-mode laser diode with a core diameter of 100 μm and numerical aperture of 0.22 was used as the pump source. The light from the laser diode was collimated and focused by a pair of 8-mm-focal-length lenses. After the coupling optics, there was about 92% pump power incident on the Cr,Yb:YAG crystal and the pump beam spot in Cr,Yb:YAG was about 100 μm in diameter. The laser spectrum was analyzed by using an ANDO AQ6317 optical spectrum analyzer. The Q-switched pulse shapes and pulse trains were recorded using a fiber-coupled InGaAs photodiode with a bandwidth of 16 GHz (rise time from 10 to 90% was 25 ps), and a 7 GHz Tektronix TDS7704B digital oscilloscope. The laser output beam profile near the output coupler and far field was monitored by a CCD camera, and the beam diameter and beam quality $M^2$ can be determined.

There is no lasing with Cr,Yb:YAG crystals doped with 0.05, 0.07 and 0.1 at. % Cr for either laser configuration, because of the strong absorption of $Cr^{4+}$ ion at 940 nm pump wavelength and the fluorescence quenching with a high Cr concentration in Cr,Yb:YAG crystal, as shown in Fig. 3. Fortunately, a self-Q-switched laser was obtained in Cr,Yb:YAG doped with 0.025 at. % Cr.[52] The initial trans-mission of $Cr^{4+}$ saturable absorber at 1.03 μm in this crystal co-doped with 0.025 at. % Cr and 10 at. % Yb is about 89%. The average output power as a function of the absorbed pump power for a plane-concave cavity Cr,Yb:YAG self-Q-switched laser is shown in Fig. 8. The absorbed pump power thresholds are about 350 and 380 mW for 2 and 5% transmission of the output coupler ($T_{oc}$), respectively. The average output power increases linearly with the absorbed pump power. However, there is coating damage for $T_{oc} = 2\%$ when the absorbed pump power is higher than 920 mW, this may be caused by the high reflectivity of the output coupler, which results in very high photon density in the laser cavity. For $T_{oc} = 5\%$, there is no coating damage even at higher pump power level, however, the average output power is saturated when the absorbed pump power is above 1 W. The highest average output power of 70 mW was measured when the absorbed pump power was about 980 mW for $T_{oc} = 5\%$, the slope efficiency was 12% and the maximum optical-to-optical efficiency was about 7%. Owing to the nature of the quasi-three-level system of $Yb^{3+}$,
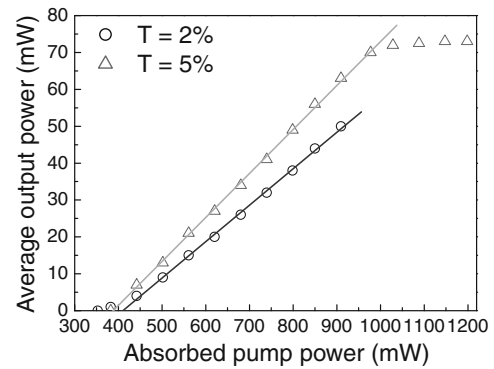


Fig. 8. Average output power of the Cr,Yb:YAG self-Q-switched laser with plane-concave cavity as a function of the absorbed pump power. The lines are the linear fits of the experimental data.

there is stronger re-absorption at laser wavelength of 1030 nm, which depends strongly on the temperature of the Cr,Yb:YAG: the higher the temperature, the stronger is the absorption. Because the optical and thermal properties of ytterbium-doped YAG crystal improve at low temperature,[31,53] efficient laser operation could be achieved by cooling the sample. The efficient operation of Yb:YAG crystal at liquid nitrogen temperature has been demonstrated.[54,55] A low threshold and highly efficient performance of Cr,Yb:YAG crystal should be achieved at low temperature.

The repetition rate increases linearly from several hundred Hz to 6.3 kHz with the absorbed pump power. The pulse width (FWHM) decreases very slowly from 15.5 to 12.3 ns with the absorbed pump power and remains constant in the higher pump power range, with much smaller difference for two transmissions of the output coupler. The pulse energy increases with the pump power, and the highest pulse energy of 7.9 and 11.2 μJ was obtained for $T_{oc} = 2$ and 5%, respectively. The highest peak power of 915 W was obtained with $T_{oc} = 5\%$. The output self-Q-switched laser beam is a transverse $TEM_{00}$ mode with a gaussian profile. The beam quality factor $M_x^2$ and $M_y^2$ values were determined to be 2.3 and 2.36, respectively. At the same time the beam diameter near the output coupler was measured as 220 μm. Mean-while, the measured laser emitting spectra showed that the self-Q-switched laser was multi-longitudinal-mode (around 1030 nm) oscillation for both transmissions of the output coupler.

Repetitive self-Q-switched laser pulse trains were ob-served when the absorbed pump power was above 680 mW for Cr,Yb:YAG monolithic microchip laser operation, the output laser pulse train was stable with further increase in the pump power, and variation of the pulse amplitude was within 5% even at lower pump power. Figure 9 shows a train of the laser pulse and the oscilloscope pulse profile at the absorbed pump power of 1.52 W, the pulse-to-pulse ampli-tude fluctuation is less than 1% [as shown in Fig. 9(a)], the repetition rate was determined to be 6.6 kHz. The self-Q-switched pulse profile with output pulse energy of 23.5 μJ and pulse duration (FWHM) of 440 ps is shown in Fig. 9(b). So the peak power is estimated to be over 53 kW. The
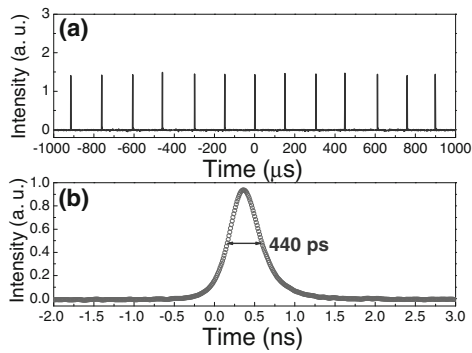
Fig. 9. (a) Laser pulse train and (b) the pulse profile of the Cr,Yb:YAG monolithic microchip laser at the absorbed pump power of 1520 mW; the pulse width (FWHM) is 440 ps; the repetition rate is 6.6 kHz.
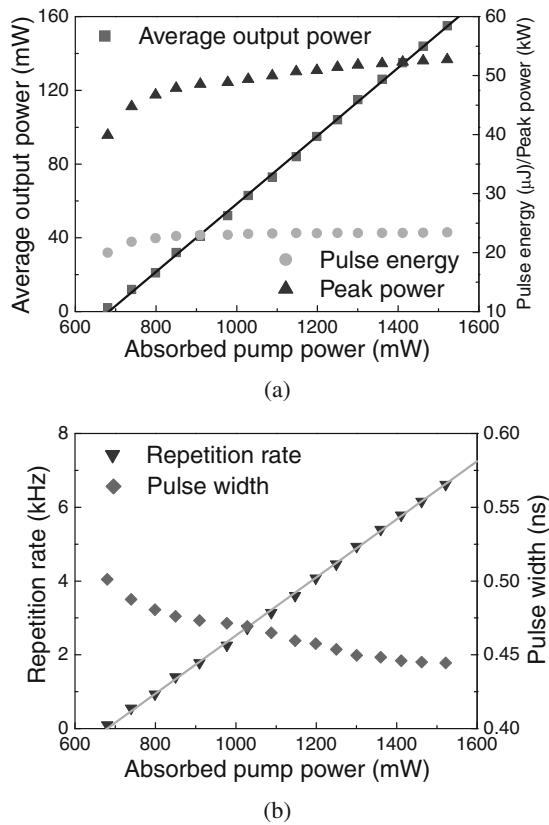


(a)



(b)

Fig. 10. (a) Average output power, pulse energy and peak power, (b) pulse width (FWHM) and repetition rate of the Cr,Yb:YAG self-Q-switched microchip laser as a function of the absorbed pump power.

average output power, pulse energy, peak power, pulse width and repetition rate as a function of the absorbed pump power is shown in Fig. 10. The average output power increases linearly with the absorbed pump power, and there is no pump saturation although the Cr,Yb:YAG crystal is not temperature controlled. Therefore, the average output power can be scaled further with higher pump power. The highest output power of 156 mW was obtained at maximum absorb-

ed pump power of 1.52 W, the slope efficiency was as high as 18.5%, the corresponding optical-to-optical efficiency was about 10%. Room temperature operation of Cr,Yb:YAG self-Q-switched laser with low-power (several watts) and a high brightness laser-diode as pump source makes this crystal a potential candidate for a compact, robust laser for some applications without a cooling system. The pulse energy increases with the pump power when the pump power is above the pump power threshold, then remains nearly constant when the absorbed pump power is over 900 mW. The peak power of Cr,Yb:YAG self-Q-switched laser increases quickly with the pump power at lower pump power range and then increases slowly at higher pump power range (above 900 mW). The repetition rate increases linearly from several hundred Hz to 6.6 kHz with the absorbed pump power. The pulse width (FWHM) decreases very slowly from 500 to 440 ps with the absorbed pump power. There was no dielectric coating damage observed even with a shorter pulse width of 440 ps throughout the laser experiments, this is attributed to the decrease of Cr concentration in Cr,Yb:YAG crystal (0.025 at. % vs 0.5 at. %[35]); the defects in the crystal introduced by the Cr concentration were decreased, while the modulation depth (initial transmission of 89%) was kept nearly the same with 1 mm thickness of Cr,Yb:YAG crystal (as that in ref. 35).

This monolithic Cr,Yb:YAG self-Q-switched microchip laser operates at multi-longitudinal modes (from two to five modes), as shown in Fig. 11. The separation of each frequency under different pump power is about 0.29 nm, in agreement with the free spectral range of a 1-mm-long laser resonator filled with gain medium predicted by[56] $\Delta\lambda_c = \lambda^2/2L_c$, where $L_c$ is the optical length of the resonator and $\lambda$ is the laser wavelength. The linewidth of each mode is measured to be 0.02 nm, limited by the resolution of the available optical spectrum analyzer. The output Q-switched pulses are linearly polarized along either of the mutually orthogonal axes, with an extinction ratio of over 30 : 1. Similar linear polarization was also observed in plane-concave Cr,Yb:YAG self-Q-switched lasers, this polarization does not change with the rotation of the Cr,Yb:YAG sample. The laser output power beam profile
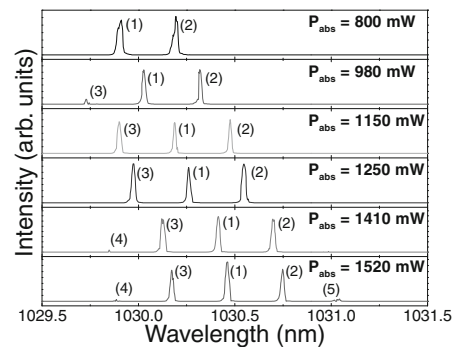


Fig. 11. Laser emitting spectra of the Cr,Yb:YAG self-Q-switched microchip laser under different pump power. The resolution of the measurement is 0.01 nm.
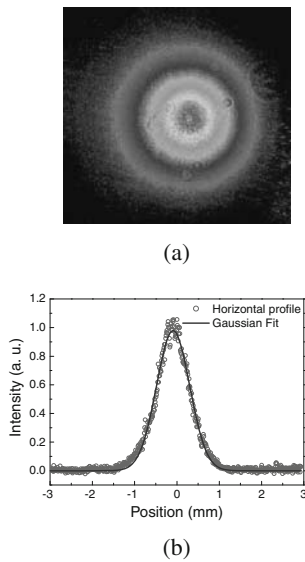
(a)



(b)

Fig. 12. (a) Measured laser output beam profile; (b) horizontal transverse beam profile with Gaussian fitting of the Cr,Yb:YAG self-Q-switched microchip laser.
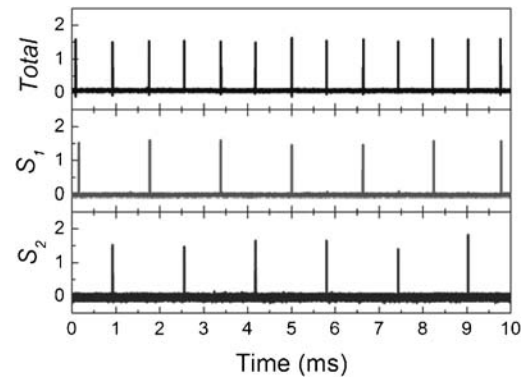


Fig. 13. Total output pulse train, and output pulse trains of each mode for the self-Q-switched Cr,Yb:YAG two-mode oscillation at the pump power ratio, $w$, of 1.2.

as well as a horizontal slice through the center are shown in Fig. 12, and the output beam well fits the Gaussian profile [Fig. 12(b)]. The beam quality factor $M_x^2$ and $M_y^2$ values were determined to be 1.17 and 1.16, respectively. Near diffraction-limited output beam quality was achieved in such a compact monolithic Cr,Yb:YAG self-Q-switched laser. The output beam diameter near the output mirror was measured as 120 μm.

Although the microchip Cr,Yb:YAG self-Q-switched laser operated in multi-longitudinal modes (as shown in Fig. 11), stable output pulse trains were obtained [as shown in Fig. 9(a)], which is attributed to the antiphase dynamics between longitudinal modes. The antiphase dynamics of the self-Q-switched Cr,Yb:YAG multimode laser was studied experimentally by measuring the contribution of each mode to the total output intensity. The measured pulse trains of each mode and the total laser output can identify the temporal behavior of the multimode laser within the antiphase regime. A typical example of the measured pulse train of self-Q-switched two-mode laser and the pulse trains of each mode was shown in Fig. 13 when the pump power ratio (absorbed pump power to the absorbed pump power threshold), $w$, was 1.2. The two modes oscillate nearly at the same intensity, showing period-1 pulsations with almost the same repetition frequency. Comparison of the total pulse repetition frequency with that of each mode shows that each mode is shifted from the next mode by about 1/2 of the period. The two modes thus operate in opposite phase alternatively competing for the gain and display a classic antiphase state. The antiphase state of this two-mode oscillation of the microchip Cr,Yb:YAG laser is caused by the cross-saturation mechanism due to the spatial hole burning coupling of the modes via population gratings and the nonlinear absorption of the $Cr^{4+}$ saturable absorber, as reported by other researchers.[57] As soon as the pump power

was increased to the three-mode regime, in which the third lasing mode began to oscillate, the mode oscillation dynamics was changed. The pulsations occurring for the first mode with the highest gain were characterized by a strong pulse following a weak pulse (the ratio of the weak pulse to the strong one was about 0.5) when the pump power ratio, $w$, was 1.7 [as shown in Fig. 14(a)]. The time interval between strong pulses or between weak pulses for the first mode was three times that for the total output pulse sequence. The pulse trains of the other two modes with lower gain were characterized as pulsations with amplitude fluctuation compared to the total output pulse train. Pulses of each mode were shifted from the next mode by one third of the period of each mode and also exhibited antiphase dynamics. The Q-switched laser was still in the three-mode oscillation regime when the pump power was further increased. Although the pulse trains from each mode became complicated with increase of the pump power, the output pulse trains of three-mode oscillation still displayed antiphase dynamics when the pump power ratio was 1.85 [as shown in Fig. 14(b)]. Actually, antiphase dynamics do not need to be periodic in each mode, and they can undergo bifurcation sequences. As the pump power was increased further, a fourth mode appeared (as shown in Fig. 11) and the repetition frequency increased;, the period of the first three modes was nearly the same as those displayed in the three-mode regime, the intensities of the fourth and the fifth modes were very small compared to the first three modes, which means that the oscillation threshold for these weak modes was very high compared to the three main modes. It should be noted that the phases of the intensity pulses of individual modes are different and give rise to self-organized antiphase dynamics. Although there was some inaccuracy in obtaining pulse trains for each mode, the tendency of alternate oscillation of each mode was obvious in the experiments. This evidence shows that the stable pulse trains are governed by mode coupling through the antiphase dynamics of different and separate mode oscillations. Numerical simulations for antiphase dynamics in Cr,Yb:YAG microchip self-Q-switched lasers were performed by adopting multi-longitudinal mode rate equations,
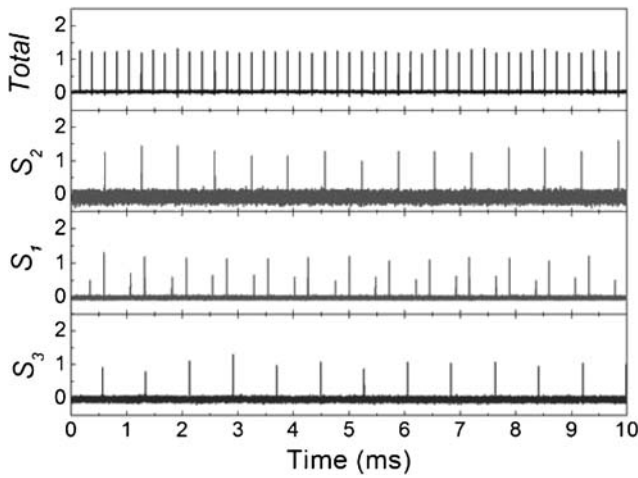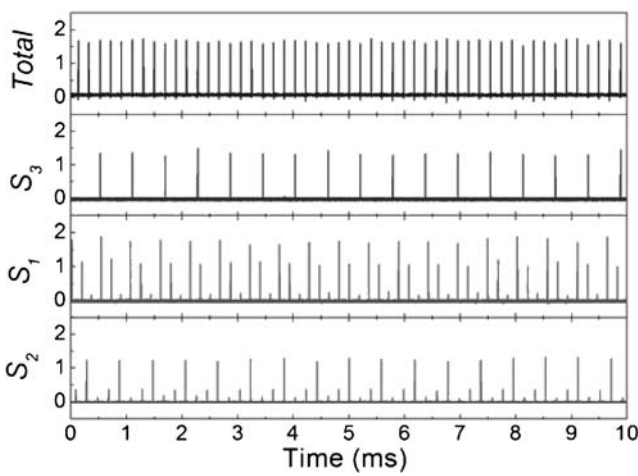
(a)



(b)

Fig. 14.   Total output pulse train, and output pulse trains of each mode for the self-Q-switched Cr,Yb:YAG three-mode oscillation at the pump power ratio, $w$, of (a) 1.7, (b) 1.85.



Fig. 15.   Numerical simulation of antiphase dynamics for the Cr,Yb:YAG self-Q-switched two-mode lasers at the pump power ratio, $w$, of 1.2.



(a)



(b)

Fig. 16.   Numerical simulation of antiphase dynamics for the Cr,Yb:YAG self-Q-switched three-mode lasers at the pump power ratio, $w$, of (a) 1.7, (b) 1.85.

taking into account the spatial hole burning effect and nonlinear absorption of $Cr^{4+}$:YAG crystal.[58] A typical numerical example of the population inversion density of the saturable absorber, $N_g$, and the population inversion density, $n_0 - n_1/2$, $n_0 - n_2/2$, and the photon density, $\phi_1$, $\phi_2$, for two-mode oscillation based on eqs. (A·1)–(A·4) is shown in Fig. 15, the pump rate $w = 1.2$, $\gamma_1 = 1$, $\gamma_2 = 0.99$, and other laser parameters used in numerical calculations are taken from ref. 59. This numerical solution of two-mode oscil- lation is quite similar to the experimental result shown in Fig. 13. The numerical simulations of the population inversion density of the saturable absorber and the popula- tion inversion density, $n_0 - n_1/2$, $n_0 - n_2/2$, $n_0 - n_3/2$ and the photon density for the three-mode oscillations with $\gamma_1 = 1$, $\gamma_2 = 0.99$, $\gamma_3 = 0.98$ under different pumping power ratios are shown in Fig. 16, which are in good agreement with the experimental results shown in Fig. 14. The antiphase states were reproduced in the numerical calculations irrespective of the initial conditions for the mode intensities and gains; the antiphase state generally
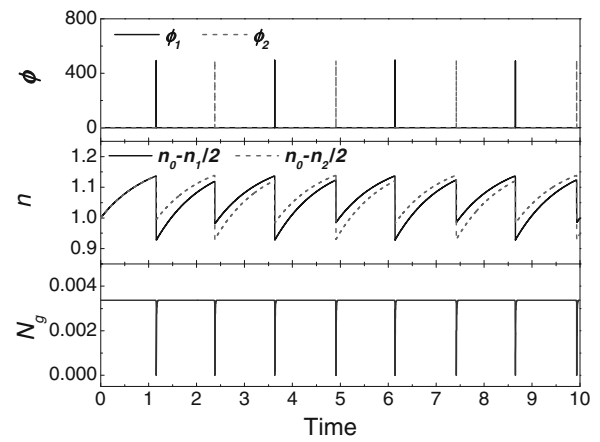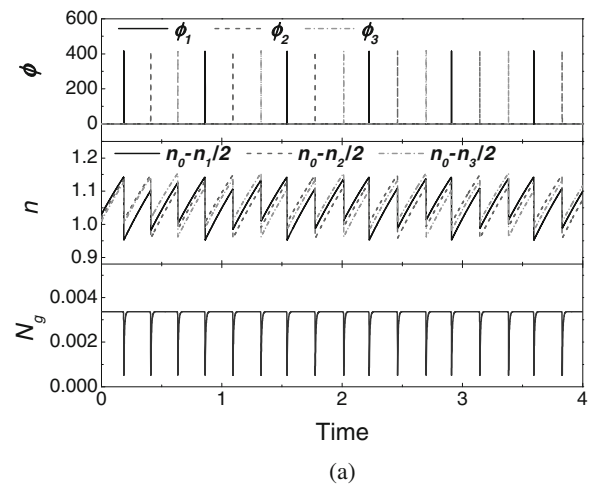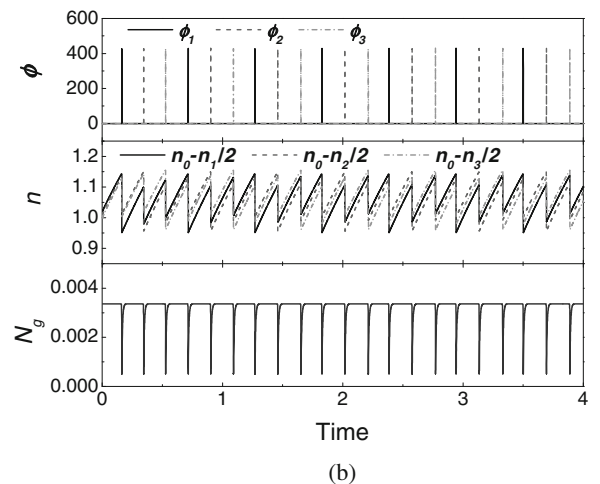
exists in this Cr,Yb:YAG self-Q-switched microchip multi-longitudinal mode lasers. The time interval between each pulse for the total output is governed by the bleaching and recovery time of the population inversion of the $Cr^{4+}$ saturable absorber. Although there are some simplifications in the numerical calculations and discrepancies between the experimental results and numerical simulations, the numerical simulations of the antiphase states for the Cr,Yb:YAG self-Q-switched laser give us a clear image of the spatial hole burning of the gain medium and the nonlinear absorption of the saturable absorber on the dynamics of the antiphase states.

### 3.2 Composite Yb:YAG/Cr:YAG ceramics microchip lasers

Firstly, the performance of composite Yb:YAG/Cr:YAG ceramic laser was investigated by using a plane-concave cavity [the experimental setup is similar to that for Cr,Yb:YAG microchip laser, as shown in Fig. 7(a)]. The gain medium is a plane-parallel, 3.5-mm-thick Yb:YAG/Cr:YAG composite ceramics, the thicknesses of Yb:YAG and Cr:YAG ceramics segments are 1.5 and 2 mm. The initial transmission of $Cr^{4+}$:YAG at 1030 nm was estimated to be 64%. One surface of the composite ceramic with Yb doping is coated for high transmission at 940 nm and total reflection at 1030 nm. The other surface is coated for antireflection at 1030 nm.

The threshold absorbed pump power was measured as 0.9 W owing to the low initial transmission of $Cr^{4+}$:YAG at 1030 nm. Average output power increased linearly with absorbed pump power above the absorbed pump power threshold. The slope efficiency was 27% corresponding to the absorbed pump power. The maximum average output power of 480 mW was measured when the absorbed pump power was 2.55 W; further increase in pump power resulted in coating damage. Self-Q-switched laser pulses with pulse energy of 125 μJ and pulse width of 1.2 ns at a repetition rate of 3.8 kHz were obtained at the absorbed pump power of 2.55 W; the corresponding peak power was over 105 kW. The pulse energy does not tend to be saturated at an absorbed pump power of 2.55 W, and high pulse energy can be obtained by increasing the transmission of the output coupler or improving the coating quality. The transverse output beam profile is close to $TEM_{00}$ mode. Near diffraction-limited output beam quality with $M_x^2$ of 1.35 and $M_y^2$ of 1.31, respectively, was achieved. Laser-induced coating damage in fused silica depends on the pulse width, the longer the pulse width, the higher the coating damage threshold.[60] For 1 ns pulse width, this threshold should be around 50 J/cm$^2$ for fused silica; however, the threshold was estimated to be 15 J/cm$^2$ based on the laser beam diameter of 120 μm and intracavity laser fluence of 1.25 mJ. Therefore, the laser performance can be further improved by enhancing the coating quality or adjusting the thickness of lasing and Q-switching parts in Yb:YAG/Cr:YAG composite ceramics.

Composite Yb:YAG/$Cr^{4+}$:YAG ceramic self-Q-switched microchip laser was demonstrated successfully by adjusting the thickness of Yb:YAG and $Cr^{4+}$:YAG parts based on the previous experiments.[61] A unitized design plane-parallel coated composite Yb:YAG/$Cr^{4+}$:YAG ceramic was used as working medium, the thickness of its Yb:YAG and $Cr^{4+}$:YAG parts were 1.2 and 1.5 mm, respectively. The reason for the short $Cr^{4+}$:YAG part was to increase the initial transmission at 1.03 μm lasing wavelength to avoid the coating damage by limiting the output energy. The initial transmission of the $Cr^{4+}$:YAG part at 1030 nm was estimated to be 70% based on the measured absorption spectra of this composite Yb:YAG/$Cr^{4+}$:YAG ceramics.[46] The experimental setup was similar to that for monolithic microchip Cr,Yb:YAG laser [Fig. 7(b)]. Surface of the ytterbium lasant segment was coated for high transmission at 940 nm and total reflection at 1030 nm lasing wavelength. The other surface of the $Cr^{4+}$:YAG segment was antireflection coated for 1030 nm lasing wavelength. A plane-parallel output coupling mirror with 50% transmission at 1030 nm was used as output coupler. The cavity length was about 2.7 mm.

Average output power of all-ceramic composite Yb:YAG/$Cr^{4+}$:YAG self-Q-switched microchip lasers as a function of the absorbed pump power and output beam profile were shown in Fig. 17. The absorbed pump power threshold was about 1.35 W, resulting from the low initial transmission of $Cr^{4+}$:YAG ($T_0 = 70$%) at 1030 nm and high transmission (50%) of the output coupler. As seen, average output power increases linearly with the absorbed pump power; the slope efficiency is about 29%. Maximum average output power of 610 mW was measured when the absorbed pump power was 3.53 W, corresponding to the optical-to-optical efficiency of 19%. No coating damage occurred with further increase of the pump power, owing to the decrease of the intracavity energy fluence. The transverse output beam profile is shown in inset (a) of Fig. 17, and is close to the $TEM_{00}$ mode. Measured position-dependent beam radii near the focus are shown in inset (b) of Fig. 17. Near diffraction-limited output laser beam quality with $M_x^2$ of 1.09 and $M_y^2$ of 1.07, respectively, was achieved as well. The output beam
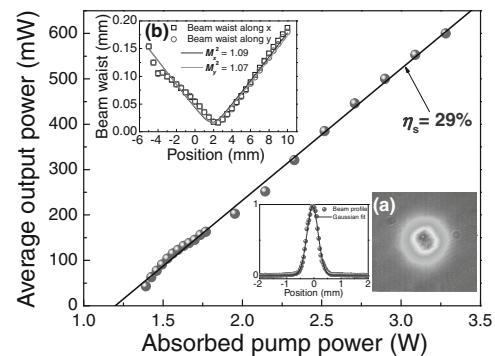


Fig. 17. Average output power as a function of the absorbed pump power for an all-ceramic composite Yb:YAG/$Cr^{4+}$:YAG self-Q-switched microchip laser. Inset (a) shows the output beam profile and transverse beam profile and (b) shows the measured beam quality factors.
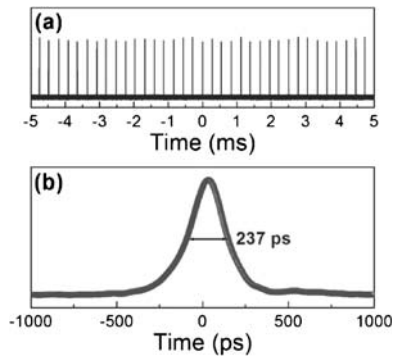
Fig. 18. (a) Oscilloscope pulse trace and (b) pulse profile with 237 ps pulse width (FWHM) and 172 μJ pulse energy of the self-Q-switched all-ceramic composite Yb:YAG/Cr$^{4+}$:YAG microchip laser, corresponding to peak power of over 0.72 MW.
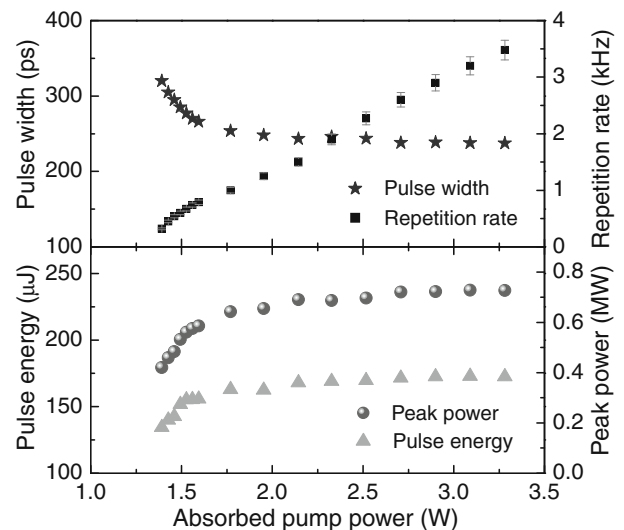


Fig. 19. Pulse characteristics (pulse energy, pulse width, repetition rate and peak power) of an all-ceramic composite Yb:YAG/Cr$^{4+}$:YAG self-Q-switched microchip laser as a function of absorbed pump power.

diameter near the output mirror was 100 μm. Single-longitudinal-mode stimulated emission oscillation at 1030.6 nm was achieved when the absorbed pump power was kept below 1.7 W. Above this value, the laser exhibited two- or three-longitudinal-modes oscillation. It should be noted that stable single-longitudinal-mode oscillation could be obtained by increasing the pump beam diameter incident on the laser ceramic at higher pump power.

Figure 18 shows the oscilloscope trace of the pulse trains and the output pulse with 237 ps pulse width (FWHM) and 172 μJ pulse energy. The output pulse amplitudes and repetition rate fluctuation are less than 6% [as shown in Fig. 18(a)], evidencing a very stable self-Q-switched laser operation. Over 0.72 MW laser pulses with the pulse width of 237 ps were obtained at a repetition rate of 3.5 kHz when the absorbed pump power is 3.35 W [as shown in Fig. 18(b)]. The unfocused peak output intensity was $>9.2 \times 10^9$ W/cm$^2$ with a lasing mode diameter of 100 μm. The focused peak output intensity will be $>10^{12}$ W/cm$^2$ with a commercial available focus lens, such high peak power intensity offers the potential for use in laser ignition, material processing, efficient nonlinear conversion, and so on. Figure 19 shows pulse repetition rate, pulse width, pulse energy, and peak power as a function of the absorbed pump power. Repetition rate increases linearly from 320 Hz to 3.5 kHz with absorbed pump power. The error bars indicate the increase of timing jitter at a high repetition rate, and the timing jitter is less than 5% even at high pump power. Pulse width (FWHM) decreases slowly from 320 to 237 ps with the absorbed pump power, while pulse energy increases from 134 to 172 μJ and tends to be saturated when the absorbed pump power is higher than 2.6 W. Peak power of this all-ceramic composite Yb:YAG/Cr$^{4+}$:YAG self-Q-switched microchip laser increases from 0.42 to over 0.72 MW with absorbed pump power. The dramatic improvement of all-ceramic composite Yb:YAG/Cr$^{4+}$:YAG self-Q-switched microchip lasers compared with those by using plane-concave cavity was due to the reduced thickness of both parts of Yb:YAG and Cr$^{4+}$:YAG, so that the reabsorption loss from Yb:YAG is decreased. Additionally, Yb:YAG ceramic is well pumped and the initial trans-

mission of Cr$^{4+}$:YAG is increased to modify the potential pulse energy generated, thereby decreasing the intracavity laser fluence to avoid coating damage. Except for the higher pump power threshold owing to the high transmission of the output coupler, the optical-to-optical efficiency and slope efficiency are comparable or better than those obtained by using a plane-concave cavity. From the improvement of the laser performance of composite Yb:YAG/Cr:YAG ceramic, we can see that the composite Yb:YAG/Cr:YAG ceramic is more suitable for generating short pulses with high peak power, because the interface between the Yb:YAG and Cr:YAG ceramics has less loss than the mechanical contact of Yb:YAG and Cr:YAG.[37] Composite Yb:YAG/Cr:YAG ceramics eliminates the absorption loss of Cr$^{4+}$ ions for pump power, which is a shortcoming of Cr,Yb:YAG self-Q-switched laser material.[26] According to the passively Q-switched solid-state laser theory,[62,63] pulse energy is proportional to the initial inversion population. The initial inversion population of passively Q-switched lasers is proportional to the losses (loss from saturable absorber, intracavity loss, and useful laser output of output coupler) before the oscillation; therefore, the pulse energy can be further increased by adjusting the initial transmission of Cr$^{4+}$:YAG saturable absorber in composite Yb:YAG/Cr:YAG ceramics.

## 4. Instability of Self-Q-switched Cr,Nd:YAG Microchip Lasers

### 4.1 TEM$_{00}$-mode oscillation

A schematic diagram of the laser-diode end-pumped TEM$_{00}$-mode Cr,Nd:YAG microchip self-Q-switched laser is shown in Fig. 20. A plane-parallel, 1-mm-thick YAG crystal co-doped with 1 at.% Nd and 0.01 at.% Cr was used as a gain medium. The planar rear surface is coated for high transmission at 808 nm and total reflection at 1064 nm to act
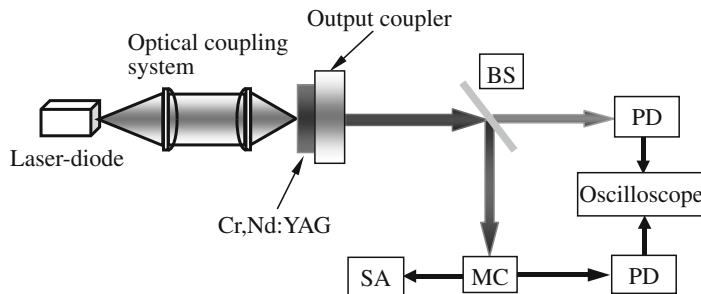
Fig. 20. Schematic diagram of TEM$_{00}$-mode Cr,Nd:YAG microchip self-Q-switched laser, BS, beam splitter; PD, photodiode; MC, monochromator; SA, spectrum analyzer.
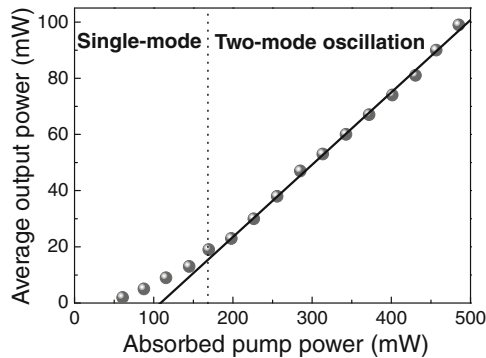


Fig. 21. Average output power of a TEM$_{00}$-mode Cr,Nd:YAG microchip self-Q-switched laser as a function of absorbed pump power.
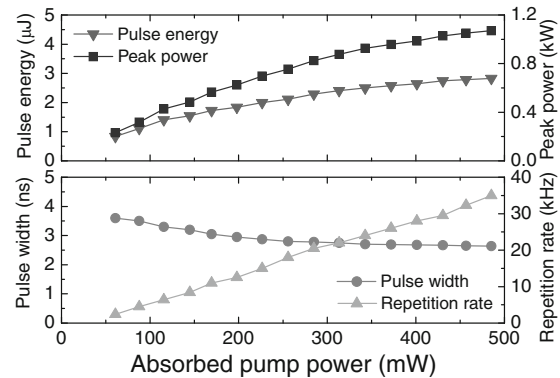


Fig. 22. Pulse width, repetition rate, pulse energy and peak power of the TEM$_{00}$-mode Cr,Nd:YAG self-Q-switched laser as a function of pump power.

as a laser cavity mirror. The planar front surface is coated for antireflection at 1064 nm and total reflection at 808 nm to increase the absorption of the pump power. A plane mirror with 5% transmission at 1064 nm was attached to the Cr,Nd:YAG crystal as a output coupler. A 1-W, continuous-wave, high-brightness 808 nm laser diode with a $50 \times 1 \, \mu m^2$ emission cross section was used as the pump source for generating TEM$_{00}$-mode oscillation. The coupling optics (two lenses with a focus length of 8 mm) was used to focus the pump beam into the crystal rear surface. After the coupling optics, there was about 70% pump power incident on the Cr,Nd:YAG crystal and the pump light footprint in crystal was about $75 \times 75 \, \mu m^2$. The laser was operated at room temperature without an active cooling system. The laser spectrum was analyzed by using an ANDO AQ6317 optical spectrum analyzer. To study the dynamics of different longitudinal modes separately and make sure the detected signal was one mode of the solitary laser, a monochromator was used as a wavelength band-pass filter to select different longitudinal modes. The pulse train of a selected mode and the total pulse train can be detected by using two photodiode detectors and a fast digital oscilloscope simultaneously. A CCD camera was used to monitor the laser output beam profile.

The average output power of a laser-diode end-pumped Cr,Nd:YAG self-Q-switched laser as a function of the absorbed pump power is shown in Fig. 21. The absorbed pump power threshold was 60 mW. Stable single longitudinal-mode oscillation was obtained when the absorbed pump

power was kept below 170 mW. Above this value, the laser exhibited two-longitudinal-mode oscillations. The slope efficiency was as high as 26% which is comparable to the Cr,Nd:YAG laser performance with Ti:sapphire laser as a pump source[64] and optical-to-optical efficiency was about 20.5%. The output laser transverse intensity profile was close to TEM$_{00}$ and was near-diffraction-limited with $M^2$ of 1.2. Figure 22 shows the pulse characteristics (pulse width, repetition rate, pulse energy, and peak power) as a function of the absorbed pump power. The repetition rate increased linearly from several kHz to 40 kHz with the absorbed pump power. Pulse width decreased, pulse energy and peak power increased with the absorbed pump power, and the pulse width and the pulse energy tending to be independent of the absorbed pump power in the higher pump power regime. A maximum average output power of 99 mW and pulse energy of 2.8 μJ with pulse duration (FWHM) of 2.6 ns at a repetition rate of 40 kHz were obtained when the absorbed pump power was 485 mW. A maximum peak power of over 1 kW was obtained.

Single-longitudinal-mode and two-longitudinal-mode oscillations (around 1064 nm) were observed in this self-Q-switched laser by measuring the output laser spectrum, the self-Q-switched laser emitting spectra at different absorbed pump power are shown in Fig. 23. Single-longitudinal-mode oscillation at 1063.86 nm was obtained. The main mode wavelength was 1063.88 nm, and secondary mode wavelength was 1064.2 nm for two-longitudinal-mode oscillation. The intensity of the secondary mode increased with the
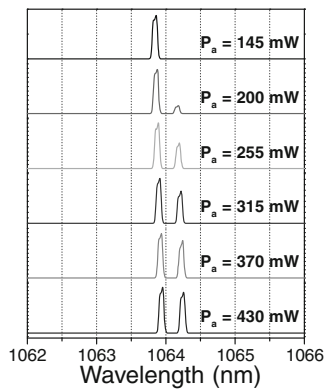
Fig. 23.   Laser emitting spectra of a Cr,Nd:YAG self-Q-switched laser at different absorbed pump power levels. Resolution of the measurement is 0.01 nm.



Fig. 24.   Evolution of the output pulse sequences at the absorbed pump power: $P_a$ = (a) 85, (b) 115, (c) 145 mW for single-mode oscillation; $P_a$ = (d) 200, (e) 255, (f) 315 mW for two-mode oscillation which show the instabilities of the pulses.



Fig. 25.   Numerical simulation of the population inversion, the population inversion of the saturable absorber and the photon intensities for two-mode oscillation at the pump power ratio $w = 3.33$. $Th_1$ and $Th_2$ are the thresholds for the first-mode and secondary-mode, respectively.

absorbed pump power; and the wavelength of each mode shifted to a longer wavelength with increase the absorbed pump power. This was caused by rise in the temperature of the gain medium: the heat generated inside the gain medium increases and the emission spectrum of Nd:YAG crystal shifts to a longer wavelength with increase in temperature.[65] The separation of two-mode oscillation under different pump power was about 0.31 nm, which is in good agreement with the free spectral range between longitudinal modes in the laser cavity filled with gain medium predicted with[56] $\Delta\lambda_c = \lambda^2/2L_c$, where $L_c$ is the optical length of the resonator and $\lambda$ is the laser wavelength. The linewidth of each mode was 0.06 nm, limited by the resolution of optical spectrum analyzer used in the experiments.

The instability dynamics of the self-Q-switched two-longitudinal-mode laser was studied experimentally by measuring the total output pulse sequence intensity. Typical examples of the measured pulse train of self-Q-switched single longitudinal-mode and two-longitudinal-mode laser at different pump powers are shown in Fig. 24. Stable single-longitudinal-mode pulses with uniform amplitude were observed and pulse repetition rate increased with the absorbed pump power as shown in Figs. 24(a)–24(c). No repetition rate jitter occurred in this single-longitudinal-mode oscillation regime. When the laser was working in a two-longitudinal-mode regime, the output pulse trains were characterized by a modulation of the pulse intensity with a period three times that of the repetition period as shown in Figs. 24(d)–24(f). The most interesting thing is that the pulsations occurred for the first mode with the highest gain characterized by two pulse oscillations of nearly equal intensity, the secondary mode with higher intensity appearing alternately with two pulse oscillations of the first mode. The time interval between the pulses varied in accordance with the pulse amplitudes; the time interval following a strong pulse was typically about 0.9 fold of those following a weak pulse. With further increase in pump power, the pulsation characteristics of the output laser do not change, but the time interval between each pulse is shortened. Obvious amplitude instability of each pulse and the repetition rate jitter were observed experimentally for the
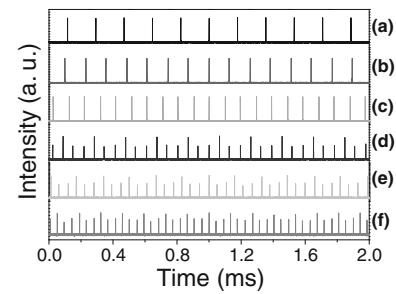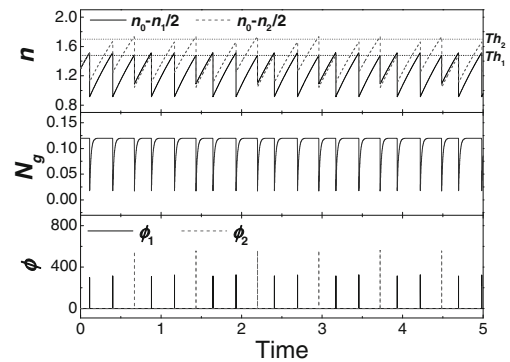
two-longitudinal-mode oscillation of a laser-diode pumped microchip Cr,Nd:YAG self-Q-switched laser.

The instability nature of the two-longitudinal-mode self-Q-switched microchip laser was investigated with the modified multimode laser rate equations [eqs. (A·1)–(A·4)] taking into account the cross-saturation dynamics that is due to the spatial hole-burning effect and the nonlinear absorption of the saturable absorber.[66] Because the gain spectrum of $Nd^{3+}$ in YAG crystal is narrow (about 1 nm at room temperature[65]) and the longitudinal mode space (0.31 nm) is wide, the loss and spontaneous emission rate are quite different for two-longitudinal-mode oscillation. A typical numerical solution of the population inversion density of two modes, $n_0 - n_1/2$, $n_0 - n_2/2$, the population inversion density of the saturable absorber, $N_g$, and the photon density for two-longitudinal-mode oscillation, $\phi_1$, $\phi_2$, are shown in Fig. 25, the pump rate $w = 3.33$, $\gamma_1 = 1$, $\gamma_2 = 0.8$; other laser parameters used in numerical calculations are taken from ref. 51. These numerical solutions of pulse repetition rate and average pulse width for two-mode oscillation reproduced the experimental results shown in Fig. 24(d). The pulse amplitude fluctuations and the repetition rate jitters were reproduced in the numerical calculations
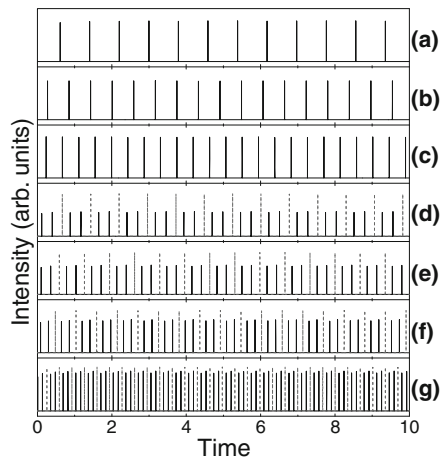
Fig. 26. Numerically calculated self-Q-switched pulse trains at different pump power ratios: $w =$ (a) 1.4, (b) 2, (c) 2.4, (d) 3.33, (e) 4.3, (f) 5.3, (g) 8. The black solid lines in (d)–(g) represent the output pulse train from the main mode and the red dashed lines represent the output pulse train from the secondary mode.



Fig. 28. Average output power and repetition rate of a Cr,Nd:YAG self-Q-switched laser as a function of the Cr,Nd:YAG sample position, $z$, along the pump beam direction.
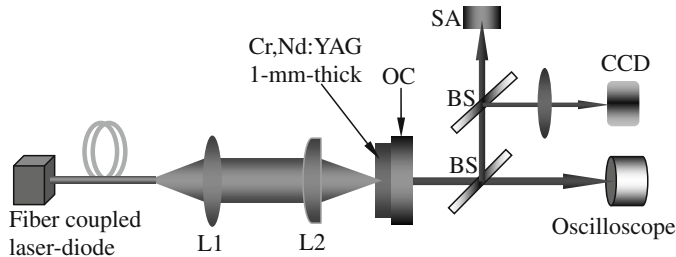


Fig. 27. Schematic diagram of a laser-diode pumped microchip Cr,Nd:YAG self-Q-switched laser to generate nanosecond transverse patterns. L1 and L2 are the focus lens; SA, spectrum analyzer; BS, beam splitter; OC, output coupler.

irrespective of the initial conditions for the mode intensities and gains; suggesting that the pulse repetition rate's jitter is also an intrinsic property of the laser system due to the spatial hole-burning effect of the gain medium and the nonlinear absorption of the saturable absorber. The similar pulsation instability dynamics of two-mode oscillation does not change with the increase of the pump power ($w$ from 2.5 to 8), however, the time interval between the pulses is shortened with the increase in pump power, as shown in Figs. 26(d)—26(g). The time interval between each pulse for the total output pulse train is governed by the bleaching and recovery time of the population inversion of the $Cr^{4+}$ saturable absorber. Numerical simulations of stable single-longitudinal-mode oscillation of Cr,Nd:YAG self-Q-switched laser were obtained by solving the rate equations, setting $N = 1$ for eqs. (A·1)–(A·4); the results are shown in Figs. 26(a)–26(c) for different pump power ratios. Stable laser operation should be achieved by increasing the pump beam diameter incident on the gain medium to realize the single-longitudinal mode oscillation.

### 4.2 Multi-transverse mode oscillations

Output power and pulse energy from a microchip Cr,Nd:YAG self-Q-switched laser can be scaled by increasing the pump beam diameter incident on the Cr,Nd:YAG crystal; the effect of pump beam diameter on the laser
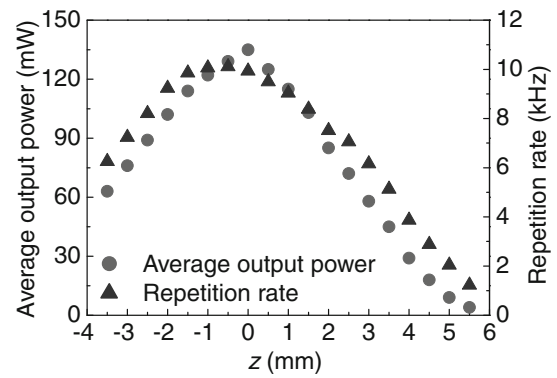
performance of Cr,Nd:YAG self-Q-switched laser was determined by varying the position of the crystal along the pump beam direction.[67] Figure 27 shows a schematic diagram of a laser-diode end-pumped microchip Cr,Nd:YAG self-Q-switched laser with large beam diameter. A 3-W fiber-coupled 807 nm laser-diode with a core diameter of 400 μm and numerical aperture of 0.4 was used as the pump source. Two lenses with focus length of 15 mm (L1) and 40 mm (L2), respectively, were used to focus the pump beam into the rear surface of the crystal and produce a pump light footprint in the crystal of about 300 μm in diameter. The pump beam diameter could be varied by moving the Cr,Nd:YAG crystal along the pump beam direction.

The Cr,Nd:YAG self-Q-switched laser was operated at 1.5 times above the pump power threshold when the focus spot of the pump beam was exactly on the rear surface of the Cr,Nd:YAG crystal. Average output power and repetition rate as a function of the Cr,Nd:YAG sample position ($z$) along the pump beam direction are shown in Fig. 28. The $z = 0$ coordinate corresponds to a minimum measured pump beam waist of 150 μm on the rear surface of the Cr,Nd:YAG crystal. Negative displacement of the Cr,Nd:YAG sample from $z = 0$ indicates that the sample is close to the focus lens (L2), while positive displacement indicates it is far from the lens (L2). The spot size of the pump beam increases almost symmetrically for both positive and negative displacements
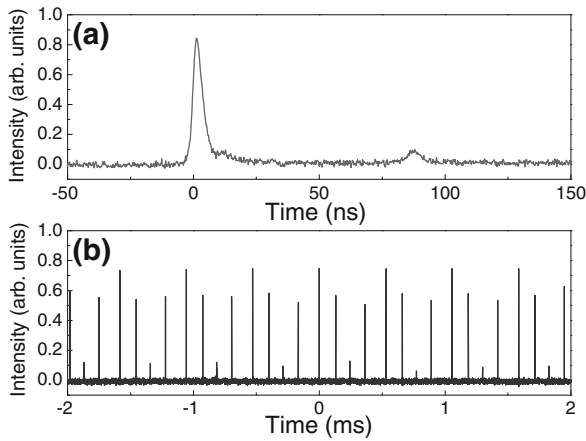
Fig. 29. (a) Typical pulse profile with two-pulse and (b) pulse train exhibiting peak power instability and repetition rate jitter at $z = 0$.

of the sample from $z = 0$. Maximum average output power of 130 mW was obtained at $z = 0$; average output power decreases by moving the Cr,Nd:YAG crystal close to or away from the focus lens (L2) along the pump beam direction. The repetition rate had the same tendency as that for average output power with the sample position, $z$, however, the maximum repetition rate was obtained at $z = -0.5$ mm. This was caused by the gain-guiding effect induced by the saturated inversion population distribution inside the Cr,Nd:YAG crystal. Maximum output pulse energy of approximately 13.6 µJ was obtained at $z = 0$, which is higher than that obtained by using a $50 \times 50 \, \mu m^2$ focus spot.[68] The output pulse of this self-Q-switched laser was multi-pulse oscillation or pulse with bifurcation. Figure 29(a) shows a typical output pulse profile with two pulses oscillating simultaneously at $z = 0$. Figure 29(b) shows a typical pulse train with periodical pulses oscillation and repetition rate jitter at $z = 0$; the pulse train exhibited period-4 pulsation. Since 1-mm-thick Cr,Nd:YAG crystal was used in the experiment, the laser was operated in the single-longitudinal-mode oscillation at the low pump power intensity as indicated in ref. 68. Therefore, pulse train instability and repetition rate jitters were attributed to the multi-transverse-mode competition induced by the nonuniform distribution of $Cr^{4+}$ saturable absorber and the gain-guiding effect induced by the saturated inversion population in Cr,Nd:YAG crystal. Pulse width (FWHM) was in the range from 3 to 6 ns with the sample position, $z$. Maximum peak power of over 4.5 kW was obtained at $z = 0$.

Figure 30 shows different sets of transverse patterns generated by moving the Cr,Nd:YAG crystal along the pump direction. All observed patterns had point symmetry, were very stable, reproducible and without variation in structure over time scales of hours. Transition between two different sets of transverse patterns was found to be sudden and abrupt with slowly and gradually moving Cr,Nd:YAG crystal along the pump beam direction. Furthermore, all observed transverse patterns were preserved in free-space propagation. The patterns were determined by the gain-guiding effect induced
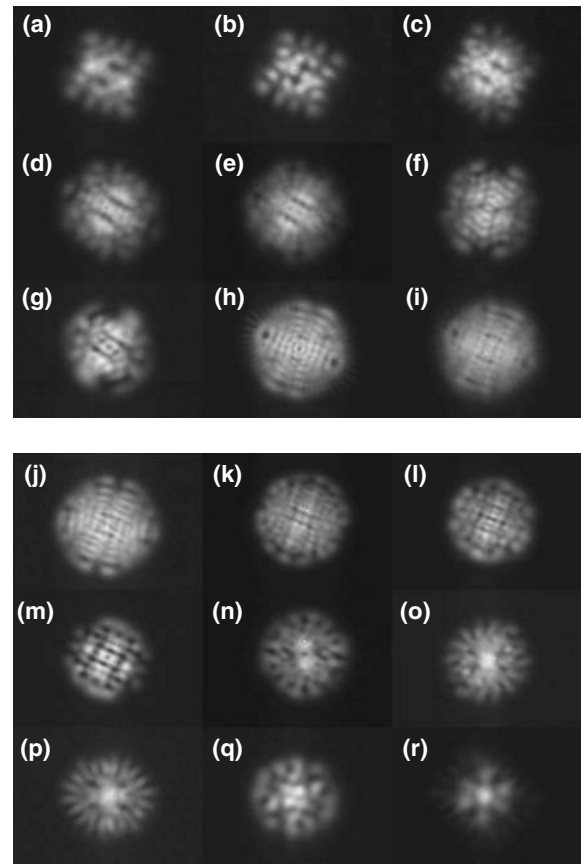


Fig. 30. Transverse patterns of a Cr,Nd:YAG self-Q-switched laser at $z =$ (a) $-3.5$, (b) $-3$, (c) $-2.5$, (d) $-2$, (e) $-1.5$, (f) $-1$, (g) $-0.5$, (h) 0, (i) 0.5, (j) 1, (k) 1.5, (l) 2, (m) 2.5, (n) 3, (o) 3.5, (p) 4, (q) 4.5, (r) 5 mm.

by the saturated inversion population distribution inside the gain medium and the nonuniform distribution of the $Cr^{4+}$ ions inside the crystal; therefore, spots and holes appear in these output patterns. This is a strong indication that the structures of the transverse patterns are actually induced by nonlinear interaction and by the spatial distribution of the pump power, and not by the configuration of the resonator. This is an intrinsic property of such microchip self-Q-switched lasers.

The oscillation criteria of the microchip Cr,Nd:YAG self-Q-switched laser were governed by the initial inversion population and the distribution of the inversion population provided by the pump power. The initial inversion population of Cr,Nd:YAG self-Q-switched laser under continuous-wave pumping can be expressed as,[69]

$$N_i = \frac{2\sigma_g \cdot N_{s0} \cdot l + \ln\left(\frac{1}{R}\right) + \delta_{\text{Loss}}}{2\sigma l} \quad (1)$$

where $\sigma$ and $\sigma_g$ are the emission cross section of gain medium and the ground-state absorption cross section of $Cr^{4+}$ saturable absorber, $N_{s0}$ is the total concentration of $Cr^{4+}$ in YAG, $l$ is the length of the Cr,Nd:YAG crystal, $R$ is the reflectivity of the output coupler, and $\delta_{\text{Loss}}$ is the total intracavity loss. The variation of the pump power
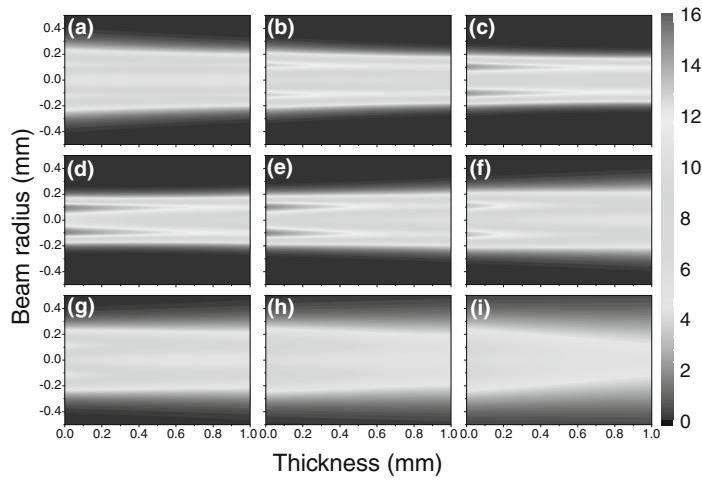
Fig. 31. Radial and longitudinal variation of the saturated inversion population inside 1-mm-thick Cr,Nd:YAG crystal at different $z =$ (a) $-3$, (b) $-2$, (c) $-1$, (d) 0, (e) 1, (f) 2, (g) 3, (h) 4, (i) 5 mm. The unit of inversion population is $\times 10^{18}$ cm$^{-3}$.

intensity on the rear surface of the gain medium with the propagation position of the pump beam can be estimated as follows,

$$I_p(z, r) = \frac{P_{in}}{\pi \cdot w_p^2(z)} \exp\left(-\frac{2r^2}{w_p^2(z)}\right) \tag{2}$$

where $z$ is the propagation direction of the pump beam, $r$ is the radius of the pump beam at $z$ position, $P_{in}$ is the incident pump power on the rear surface of the gain medium, and $w_p(z)$ is the beam waist at $z$ position of the pump beam. When the pump beam incident on the gain medium is assumed to be a Gaussian beam, using a beam quality factor, $M^2$, the radius of the pump beam along the pump direction can be expressed as,[70]

$$w_p^2(z) = w_{p0}^2\left[1 + \frac{(M^2)^2 \lambda_p^2(z - z_0)^2}{n^2 \pi^2 w_{p0}^4}\right] \tag{3}$$

where $w_{p0}$ is the waist of the pump beam at $z = z_0$; here, $z_0$ is set to 0, $\lambda_p$ is the pump wavelength, and $n$ is the refractive index of the gain medium.

For a microchip laser gain medium pumped by longitudinally continuous-wave incident pump power $P_{in}$ in a two-pass pumping scheme, the spatial distribution of the inversion population can be expressed as

$$\Delta N(r, z) = \frac{2P_{in}\alpha f \tau}{h\nu_p \pi w_p^2(z)} \exp\left(\frac{-2r^2}{w_p^2(z)}\right) \tag{4}$$
$$\times \{\exp(-\alpha z) + \exp[-\alpha(2l - z)]\}$$

where $h$ is the Planck constant, $\nu_p$ is the frequency of the pump power, $\tau$ is the fluorescence lifetime of gain medium, $\alpha$ is the absorption coefficient of gain medium at pump wavelength $\lambda_p$, $l$ is the length of the gain medium, $f$ is the thermal population distribution fraction of the upper laser level in the crystal field component (1 for a four-level system), and $w_p(z)$ is the beam waist at pump beam position $z$.

Therefore, the saturated inversion population can be expressed as follows,

$$N_{sat}(r, z, \lambda) = \Delta N(r, z)/\{1 + [I_L(r, z)/I_{sat}(\lambda)]\} \tag{5}$$

where $I_{sat}(\lambda)$ is the laser saturation intensity of the gain medium and $I_L(r, z)$ is the intensity of the laser mode inside the cavity, $I_L(r, z)$ can be expressed as,[70]

$$I_L(r, z) = \frac{4P_c}{\pi w_L^2(r, z)} \exp\left(-\frac{2r^2}{w_L^2(r, z)}\right) \tag{6}$$

where $P_c$ is the intracavity laser power, and $w_L(r, z)$ is the intracavity laser beam waist. The saturated inversion population distribution inside 1-mm Cr,Nd:YAG crystal as a function of the thickness of the crystal and pump beam radius is shown in Fig. 31. The saturated inversion population has a characteristic local minimum on the axis because the laser beam waist is experimentally observed to be smaller than the pump beam radius incident on the rear surface of the crystal; this has an important implication for the gain-guiding effect on the transverse modes. The pump area of Cr,Nd:YAG crystal was highly excited at $z = 0$, and the saturated inversion population inside the crystal was higher than the initial inversion population required by the Cr,Nd:YAG self-Q-switched laser; therefore, numericous transverse modes were excited, as shown in Fig. 30(h). Moving the Cr,Nd:YAG crystal further away from the focus point until $z = 1$ mm, the transverse patterns change little [see Fig. 30(j)] because the saturated inversion population inside the Cr,Nd:YAG decreased gradually and only the population at the edge of the pump area was lower than the initial inversion population required by Cr,Nd:YAG self-Q-switched laser; the weak oscillating modes at the edge of the output beam, therefore, had vanished. The saturated inversion population decreased further and its distribution became flatter compared to the tightly focused situation when $z > 1$ mm. Therefore, the laser will oscillate only at those pumped areas with inversion population higher than the initial inversion population required by the Cr,Nd:YAG self-Q-switched laser. The longitudinal saturated inversion population distribution inside the Cr,Nd:YAG crystal also had an effect on the transverse pattern formation, although 1-mm-thick Cr,Nd:YAG crystal was used in the experiment. Different saturated inversion population distribution along the thickness of Cr,Nd:YAG crystal at different $z$ governs different transverse pattern formation.

The observed transverse patterns exhibit rectangular structures at $z < -2$ mm and are different from high-order Laguerre–Gaussian modes. It is well-known that only Hermite–Gaussian modes retain Hermite–Gaussian field patterns as they propagate; therefore, the observed transverse patterns can be reconstructed by summing different sets of the Hermite–Gaussian modes. These modes at different positions inside the gain medium can be expressed as follows,

$$HG_{m,n}(x,y) = \frac{1}{\sqrt{2^{m+n-1}\pi m! n!}} \frac{1}{w_L} H_m\left(\frac{\sqrt{2}x}{w_L}\right) H_n\left(\frac{\sqrt{2}y}{w_L}\right)$$
$$\times \exp\left(-\frac{x^2+y^2}{w_L^2}\right)\exp(-ikz) \qquad (7)$$

where $x$ and $y$ are the Cartesian coordinates, $w_L$ is the beam waist of the laser, and $H_m$ represents a Hermite polynomial of order $m$. Here, some examples are given to illustrate the numerical reconstruction of the observed transverse patterns. The pattern observed at $z = -3$ mm can be decomposed into $|HG_{1,0} + HG_{0,2} + HG_{3,4}|^2$, as shown in Fig. 32(a). When the Cr,Nd:YAG crystal was set at $z = -2.5$ mm, the pump power induced saturated inversion population increased, allowing more modes to be excited; the transverse pattern observed in Fig. 30(c) can be decomposed into $|HG_{0,1} + HG_{2,0} + HG_{1,3} + HG_{4,4}|^2$, as shown in Fig. 32(b). When the Cr,Nd:YAG crystal was set to the focus spot of the pump beam, the saturated inversion population increased and excited more oscillating modes, therefore, the transverse patterns observed around this spot can be decomposed into more complicated oscillating modes $|HG_{1,13} + HG_{2,12} + HG_{3,11} + HG_{5,9} + HG_{7,7} + HG_{9,5} + HG_{11,3} + HG_{12,2} + HG_{14,0}|^2$, as shown in Fig. 32(c). Moving the crystal further away from the focus point of pump beam, the inversion population decreased and the oscillating modes decreased [see Figs. 32(d) and 32(e)]. Figure 32(f) shows the reconstruction of the observed transverse pattern at $z = 5$ mm by $|HG_{0,0} + HG_{1,2} + 0.5HG_{4,4}|^2$. The transverse pattern formation in microchip Cr,Nd:YAG will be strongly governed by the distribution of the gain along the radius and longitudinal direction. Especially, the longitudinal distribution of the saturated inversion population plays a very important role in the final transverse pattern formation.

The experimental and theoretical results of self-Q-switched solid-state lasers with Cr$^{4+}$:YAG as saturable absorber show that Cr$^{4+}$ ions in these lasers acts not only as saturable absorbers, but also as spatial and spectral filters. The longitudinal mode oscillations are determined by the etalon effect of Cr$^{4+}$:YAG combined with the thin gain medium of Nd or Yb doped materials. Transverse mode oscillations of self-Q-switched solid-state lasers are also governed by the distribution of Cr$^{4+}$ ions in co-doped self-Q-switched laser materials.

## 5. Conclusions

In summary, optical properties of self-Q-switched laser materials Cr,Yb:YAG, Cr,Nd;YAG and composite Yb:YAG/Cr:YAG ceramics were measured and compared.
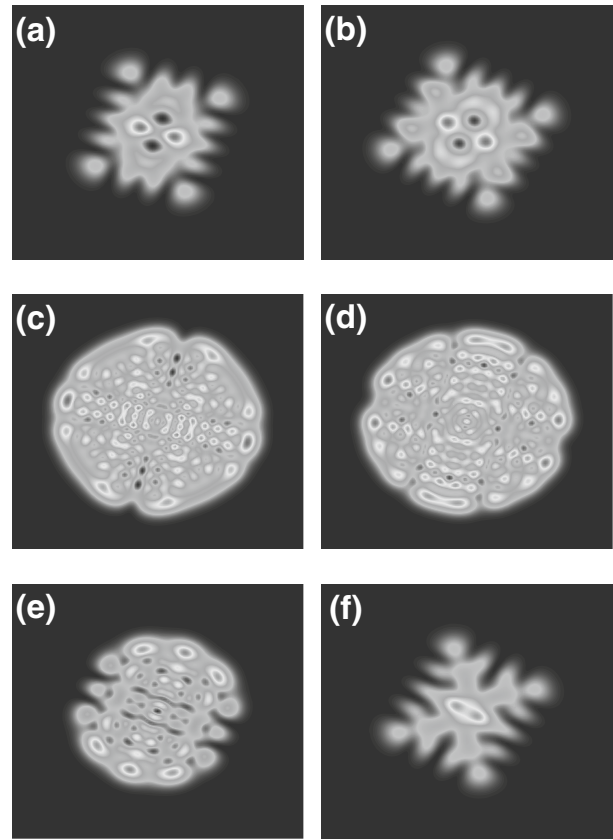


Fig. 32. Numerical reconstruction of the observed complex transverse patterns in laser-diode pumped Cr,Nd:YAG self-Q-switched microchip laser: $z = $ (a) $-3$, (b) $-2.5$, (c) 0, (d) 1.5, (e) 2.5, (f) 5 mm.

The effect of Cr$^{4+}$ ions on optical properties of co-doped Cr,Yb:YAG and Cr,Nd:YAG were addressed. Additionally, the broad absorption band of Cr$^{4+}$ ions was found to have stronger absorption of pump power for Cr,Yb:YAG than for Cr,Nd:YAG crystal, the fluorescence lifetime of Cr,Yb:YAG crystal was shortened by introduction of Cr ions, and Cr,Yb:YAG crystal had a severe fluorescence quenching effect with Cr concentration. Although laser-diode pumped Cr,Yb:YAG self-Q-switched microchip lasers with sub-nanosecond pulse width and peak power of several tens of kW were achieved, the laser pulse energy cannot be further scaled by increasing the Cr concentration because of its strong fluorescence quenching effect. For Cr,Nd:YAG self-Q-switched laser materials, the pulse energy can be scaled by increasing Cr concentration, however, the efficiency is low because defects increase with Cr concentration in Cr,Nd:YAG crystal. Stable multi-longitudinal mode laser oscillation owing to antiphase dynamics from the Cr,Yb:YAG microchip laser with nearly diffraction limited beam quality still makes the Cr,Yb:YAG self-Q-switched laser a potential candidate for material processing and other applications.

A highly efficient picosecond self-Q-switched microchip laser on the base of a novel all-ceramic composite Yb:YAG/Cr$^{4+}$:YAG structure has been developed by adjusting

thicknesses of Yb:YAG and Cr$^{4+}$:YAG parts of its binary lasing element. Laser pulses with $172\,\mu$J pulse energy and 237 ps pulse width at a repetition rate of 3.5 kHz were achieved. Over 0.72 MW peak power with a nearly diffraction-limited ($M^2 < 1.09$) lasing beam has also been demonstrated. Performance of an all-ceramic composite Yb:YAG/Cr$^{4+}$:YAG picosecond laser can be further improved by controlling concentrations of lasing (Yb) and Q-switching (Cr) coactivators, as well as by optimizing the thickness ratio of its binary parts. Compared to Cr,Yb:YAG co-doped crystals, composite Yb:YAG/Cr:YAG ceramics look very promising for generating high pulse energy and high peak power.

Although stable laser pulses from Cr,Nd:YAG self-Q-switched lasers can be obtained when the laser oscillates in single longitudinal-mode and single-transverse mode, in most cases, the laser oscillates with instabilities such as repetition jitter and pulse intensity fluctuation. The experimental results and numerical simulations of two-longitudinal-mode oscillations of Cr,Nd:YAG self-Q-switched lasers show that the instabilities caused by longitudinal mode competition is an intrinsic property of multi-longitudinal-mode Cr,Nd:YAG self-Q-switched lasers.

The laser pulse energy and output power can be scaled by increasing the pump beam diameter; however, the laser will oscillate in high-order transverse modes. The observed point-symmetric transverse patterns in a Cr,Nd:YAG self-Q-switched laser were very stable and preserved when the laser beam propagated in free space. Transverse pattern formations in this laser were mainly governed by the saturated inversion population distribution along the radius and longitudinal direction inside the Cr,Nd:YAG crystal and the initial inversion population required by the Cr,Nd:YAG laser. The observed transverse patterns were successfully reconstructed by summing different sets of Hermite–Gaussian modes. The output beam with different transverse patterns and peak power of several kW is a good candidate to generate light fields with a nontrivial transverse distribution of quantum fluctuations and can be useful in increasing the transverse resolution in optical image processing.

### Acknowledgements

### Appendix

The modified rate equations for self-Q-switched lasers of $N$ longitudinal modes with the same transverse mode structure including nonlinear absorption of the saturable absorber are introduced as follows:[66]

$$\frac{dn_0}{dt} = w - n_0 - \sum_{i=1}^{N} \gamma_i \left( n_0 - \frac{n_i}{2} \right) \phi_i \tag{A·1}$$

$$\frac{dn_i}{dt} = \gamma_i n_0 \phi_i - n_i \left( 1 + \sum_{i=1}^{N} \gamma_i \phi_i \right) \tag{A·2}$$

$$\frac{d\phi_i}{dt} = K \left[ \left\{ \gamma_i \left( n_0 - \frac{n_i}{2} \right) - 1 - 2[\delta_1 N_g - \delta_2(N_0 - N_g)]l_s \right\} \phi_i + \varepsilon n_0 \right] \tag{A·3}$$

$$\frac{dN_g}{dt} = (N_0 - N_g)\xi - \delta_1 N_g \sum_{i=1}^{N} \phi_i \tag{A·4}$$

with $i = 1, \ldots, N$. In eqs. (A·1)–(A·4), time is normalized to the fluorescence lifetime $\tau$ of gain medium,; $w$ is the relative pump rate normalized to the first-lasing-mode absorbed pump power threshold; $n_0$ is the space average of the population inversion density normalized to the first-lasing-mode threshold population inversion density, $n_i$ is the normalized Fourier components of the population inversion density for the $i$-th mode normalized to the first-lasing-mode threshold population inversion density, which can be described as follows:

$$n_0 = \frac{1}{L_c} \int_0^{L_c} n(z,t)dz \tag{A·5}$$

$$n_i = \frac{2}{L_c} \int_0^{L_c} n(z,t)\cos(2k_iz)dz \tag{A·6}$$

where $k_i$ is the wave number of mode $i$ and $L_c$ is the length of the cavity filled with active medium; $\phi_i$ is the normalized photon density, $\gamma_i \leq 1$ is the relative gain with respect to the first lasing mode, $K = \tau/\tau_c$ is the lifetime ratio of the fluorescence lifetime of the gain medium and the photon lifetime inside the laser cavity, $l_s$ is the length of the saturable absorber, $\varepsilon$ is the spontaneous emission coefficient, and $\delta_1$ and $\delta_2$ are the ratio of the ground absorption cross section and the excited state absorption cross section of Cr$^{4+}$ saturable absorber to the stimulated emission cross section of the gain medium, respectively. $N_g$, $N_0$ are the population inversion density and the total population density of Cr$^{4+}$ saturable absorber normalized to the first-lasing-mode threshold, and $\xi$ is the ratio of the fluorescence lifetime of gain medium to the lifetime of the saturable absorber.

### References

1) J. J. Zayhowski and C. Dill III: Opt. Lett. **19** (1994) 1427.
2) G. J. Spuhler, R. Paschotta, M. P. Kullberg, M. Graf, M. Moser, E. Mix, G. Huber, C. Harder, and U. Keller: Appl. Phys. B **72** (2001) 285.
3) J. Dong, P. Deng, Y. Liu, Y. Zhang, J. Xu, W. Chen, and X. Xie: Appl. Opt. **40** (2001) 4303.
4) B. Braun, F. X. Kartner, G. Zhang, M. Moser, and U. Keller: Opt. Lett. **22** (1997) 381.
5) A. A. Lagatsky, A. Abdolvand, and N. V. Kuleshov: Opt. Lett. **25** (2000) 616.
6) B. Braun, F. X. Kartner, U. Keller, J. P. Meyn, and G. Huber: Opt. Lett. **21** (1996) 405.
7) J. J. Zayhowski: J. Alloys Compd. **303–304** (2000) 393.
8) O. A. Buryy, S. B. Ubiszkii, S. S. Melnyk, and A. O. Matkovshii: Appl. Phys. B **78** (2004) 291.
9) H. Eilers, U. Hommerich, S. M. Jacobsen, W. M. Yen, K. R. Hoffman, and W. Jia: Phys. Rev. B **49** (1994) 15505.
10) R. Feldman, Y. Shimony, and Z. Burshtein: Opt. Mater. **24** (2003) 333.

11) Y. Kalisky, L. Kravchik, and M. R. Kokta: Opt. Mater. **24** (2004) 607.
12) J. Dong, P. Deng, Y. Lu, Y. Zhang, Y. Liu, J. Xu, and W. Chen: Opt. Lett. **25** (2000) 1101.
13) S. Zhou, K. K. Lee, and Y. C. Chen: Opt. Lett. **18** (1993) 511.
14) P. Wang, S. Zhou, K. K. Lee, and Y. C. Chen: Opt. Commun. **114** (1995) 439.
15) G. Yao, S. Zhou, P. Wang, K. K. Lee, and Y. C. Chen: Opt. Commun. **114** (1995) 101.
16) S. Li, S. Zhou, P. Wang, Y. C. Chen, and K. K. Lee: Opt. Lett. **18** (1993) 203.
17) V. G. Ostroumov, F. Heine, S. Kuck, G. Huber, V. A. Mikhailov, and I. A. Shcherbakov: Appl. Phys. B **64** (1997).
18) T. T. Kajava and A. L. Gaeta: Opt. Commun. **137** (1997) 93.
19) Y. F. Chen: IEEE Photonics Technol. Lett. **9** (1997) 1481.
20) N. Pavel, J. Saikawa, and T. Taira: Opt. Commun. **195** (2001) 233.
21) T. Taira, Y. Matsuoka, H. Sakai, A. Sone, and H. Kan: CLEO/QELS Conf. 2006, Long Beach, California, USA, 2006, p. CWF6.
22) J. J. Zayhowski: IEEE Photonics Technol. Lett. **9** (1997) 925.
23) J. J. Zayhowski: Opt. Mater. **11** (1999) 255.
24) J. Dong, P. Deng, and J. Xu: J. Cryst. Growth **203** (1999) 163.
25) J. Dong, P. Deng, and J. Xu: Opt. Mater. **14** (2000) 109.
26) J. Dong and P. Deng: J. Phys. Chem. Solids **64** (2003) 1163.
27) J. Dong, P. Deng, Y. Liu, Y. Zhang, G. Huang, and F. Gan: Chin. Phys. Lett. **19** (2002) 342.
28) D. S. Sumida and T. Y. Fan: Opt. Lett. **19** (1994) 1343.
29) T. Y. Fan: IEEE J. Quantum Electron. **29** (1993) 1457.
30) H. W. Bruesselbach, D. S. Sumida, R. A. Reeder, and R. W. Byren: IEEE J. Sel. Top. Quantum Electron. **3** (1997) 105.
31) J. Dong, M. Bass, Y. Mao, P. Deng, and F. Gan: J. Opt. Soc. Am. B **20** (2003) 1975.
32) F. D. Patel, E. C. Honea, J. Speth, S. A. Payne, R. Hutcheson, and R. Equall: IEEE J. Quantum Electron. **37** (2001) 135.
33) C. Stewen, K. Contag, M. Larionov, A. Giessen, and H. Hugel: IEEE J. Sel. Top. Quantum Electron. **6** (2000) 650.
34) T. Y. Fan and J. Ochoa: IEEE Photonics Technol. Lett. **7** (1995) 1137.
35) Y. Zhou, Q. Thai, Y. C. Chen, and S. Zhou: Opt. Commun. **219** (2003) 365.
36) J. Dong, A. Shirakawa, S. Huang, Y. Feng, T. Takaichi, M. Musha, K. Ueda, and A. A. Kaminskii: Laser Phys. Lett. **2** (2005) 387.
37) J. Dong, A. Shirakawa, and K. Ueda: Appl. Phys. B **85** (2006) 513.
38) G. J. Spuhler, R. Paschotta, R. Fluck, B. Braun, M. Moser, G. Zhang, E. Gini, and U. Keller: J. Opt. Soc. Am. B **16** (1999) 376.
39) T. Yanagitani, H. Yagi, and Y. Hiro: Japan Patent 10-101411 (1998).
40) H. Yagi, T. Yanagitani, K. Yoshida, M. Nakatsuka, and K. Ueda: Jpn. J. Appl. Phys. **45** (2006) 133.
41) H. Yagi, K. Takaichi, K. Hiwada, K. Ueda, and T. Yanagitani: Jpn. J. Appl. Phys. **45** (2006) L207.
42) H. Yagi, J. F. Bisson, K. Ueda, and T. Yanagitani: J. Lumin. **121** (2006) 88.
43) D. Kracht, M. Frede, R. Wilhelm, and C. Fallnich: Opt. Express **13** (2005) 6212.
44) J. Dong, A. Shirakawa, K. Takaichi, K. Ueda, H. Yagi, T. Yanagitani, and A. A. Kaminskii: Electron. Lett. **42** (2006) 1154.
45) J. Dong, A. Shirakawa, K. Ueda, H. Yagi, T. Yanagitani, and A. A. Kaminskii: Appl. Phys. Lett. **90** (2007) 131105.
46) J. Dong, A. Shirakawa, K. Ueda, H. Yagi, T. Yanagitani, and A. A. Kaminskii: Appl. Phys. Lett. **90** (2007) 191106.
47) R. D. Shannon: Acta Crystallogr., Sect. A **32** (1976) 751.
48) A. G. Okhrimchuk and A. V. Shestakov: Opt. Mater. **3** (1994) 1.
49) L. Lv, L. Wang, P. Fu, X. Chen, Z. Zhang, V. Gaebler, D. Li, B. Liu, H. J. Eichler, S. Zhang, A. Liu, and Z. Zhu: Opt. Lett. **26** (2001) 72.
50) X. B. Chen, L. Wang, J. G. Zhu, L. Lv, Z. G. Zhang, G. Z. Yang, W. Du, and D. Zhang: Opt. Eng. **43** (2004) 1350.
51) J. Dong, P. Deng, and M. Bass: Opt. Laser Technol. **34** (2002) 589.
52) J. Dong and P. Deng: Opt. Commun. **220** (2003) 425.
53) S. Zhao, A. Rapaport, J. Dong, B. Chen, P. Deng, and M. Bass: Opt. Mater. **27** (2005) 1329.
54) T. Shoji, S. Tokita, J. Kawanaka, M. Fujita, and Y. Izawa: Jpn. J. Appl. Phys. **43** (2004) L496.
55) D. J. Ripin, J. R. Ochoa, R. L. Aggarwal, and T. Y. Fan: Opt. Lett. **29** (2004) 2154.
56) W. Kochner: *Solid State Laser Engineering* (Springer-Verlag, Berlin, 1999) p. 236.
57) M. A. Larotonda, A. M. Yacomotti, and O. E. Martinez: Opt. Commun. **169** (1999) 149.
58) J. Dong, A. Shirakawa, and K. Ueda: Eur. Phys. J. D **39** (2006) 101.
59) J. Dong and P. Deng: J. Lumin. **104** (2003) 151.
60) B. C. Stuart, M. D. Feit, A. M. Rubenchik, B. W. Shore, and M. D. Perry: Phys. Rev. Lett. **74** (1995) 2248.
61) J. Dong, K. Ueda, A. Shirakawa, H. Yagi, T. Yanagitani, and A. A. Kaminskii: Opt. Express **15** (2007) 14516.
62) J. J. Degnan: IEEE J. Quantum Electron. **31** (1995) 1890.
63) J. J. Degnan: IEEE J. Quantum Electron. **25** (1989) 214.
64) J. Dong, P. Deng, and M. Bass: Opt. Laser Technol. **34** (2002) 589.
65) J. Dong, A. Rapaport, M. Bass, F. Szipocs, and K. Ueda: Phys. Status Solidi A **202** (2005) 2565.
66) C. L. Tang, H. Statz, and G. Demars: J. Appl. Phys. **34** (1963) 2289.
67) J. Dong and K. Ueda: Phys. Rev. A **73** (2006) 053824.
68) J. Dong and K. Ueda: Appl. Phys. Lett. **87** (2005) 151102.
69) J. Dong, J. Lu, and K. Ueda: J. Opt. Soc. Am. B **21** (2004) 2130.
70) T. Taira, J. Saikawa, T. Kobayashi, and R. L. Byer: IEEE J. Sel. Top. Quantum Electron. **3** (1997) 100.